NTNU

Norwegian University of
Science and Technology

Stability and compatibility of fuel cells based on proton conducting materials

Inger Marie Bjørnevik

Materials Technology

Submission date: July 2011

Supervisor: Hilde Lea Lein, IMTE
Co-supervisor: Vegar Øygarden, IMT
Mari-Ann Einarsrud, IMT
Tor Grande, IMT

Norwegian University of Science and Technology
Department of Materials Science and Engineering

Declaration

Jeg erklærer herved at diplomoppgaven har blitt utført selvstendig og i samsvar med reglementet for sivilarkitekt- og sivilingeniøreksamen ved Norges Teknisk Naturvitenskaplige Universitet.

_____ _____

Dato, sted Inger Marie Bjørnevik

Preface

This master thesis was carried out at the Department of Material Science and Engineering at the Norwegian University of Science and Technology (NTNU), spring 2011.

The master thesis is a continuation of the project "Stability and compatibility of cathodes in proton conducting SOFC" carried out by the author at NTNU, fall 2010. Some sections and parts of sections of this master thesis are collected from that work.

I would like to thank my supervisors Associate Professor Hilde Lea Lein, Professor Tor Grande, Professor Mari-Ann Einarsrud and Phd-student Vegar Øygarden for guidance and support. At last, I want to thank Julian R. Tolchard for input and guidance with SEM.

Abstract

Stability and compatibility of the proton conducting electrolyte material La_6WO_{12} with the potential cathode materials $LaCoO_3$ and La_2NiO_4 were investigated by means of solid-solid diffusion couples. Reactivity studies were carried out at 1450 °C for various times. Reaction products were analysed by SEM and EDS. The study suggests a high reactivity between the electrolyte and the electrodes, which is detrimental for the fuel cell system.

In the case of $LaCoO_3$ as a cathode material a secondary phase of $LaCo_{1-x}W_xO_3$ were formed at the interface and as precipitates in La_6WO_{12}. Theoretical models for both diffusion or interface controlled reactions failed to fit the experimental data. This failure is probably related to the reaction going towards equilibrium after a certain time, or poor connectivity between the materials.

The solid- state reaction between La_6WO_{12} and La_2NiO_4 showed formation of a composite layer of La_2O_3 and La_6WO_{12} at the interface. The reaction kinetics of this product layer was diffusion controlled. In addition to the interface reaction, precipitates of La_2O_3 and La_6WO_{12} were formed in the La_2NiO_4 phase.

Table of contents

1. Introduction

One of the more promising possibilities for future energy generation is the solid oxide fuel cell (SOFC). The solid oxide fuel cell converts the chemical energy of a fuel into electricity. It is a complete solid-state device that consists of two electrodes, an anode and a cathode, separated by an electrolyte. The electrolyte is a ceramic oxide material, which is either oxide ion conducting or proton conducting. The electrodes are also of ceramic materials or a mixture of ceramic and metallic phases. Traditionally the electrolyte in SOFCs has been an oxide ion conducting membrane operating in the temperature range from 800 to 1000 °C [1], but currently new technology has been merging with proton conducting solid oxide electrolytes (PC-SOFC). A schematic drawing of the electrode and electrolyte system of a proton conducting SOFC is illustrated in Figure 1.1. The fuel such as H_2 or other hydrocarbons is oxidized at the anode, producing electrons and ions. The H^+ species produced are then transported through the ceramic electrolyte to the cathode where, in the presence of oxygen and electrons from the external circuit, they react with O_2 molecules leading to the formation of water. [2]

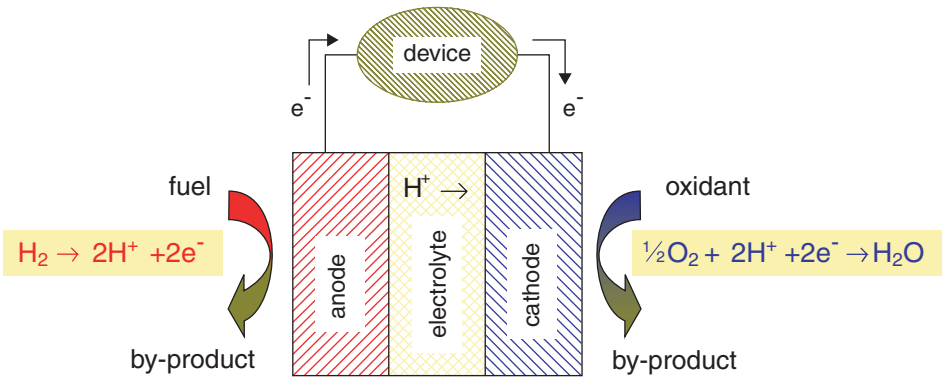

Figure 1.1 Schematic drawing of the electrode and electrolyte system of a SOFC [2].

The proton conductor offers an advantage toward its oxide-ion conducting counterpart because the migration kinetics are faster, making the cell able to run at lower temperatures (500-600 °C[1]).[3] Operating the fuel cell at a lower temperature is attractive as it improves device lifetime and reduces manufacturing costs [4]. Lower service temperatures also open up the possibility of using metallic interconnectors

instead of ceramic ones, which besides lower costs and easier fabricability, also have the advantage of higher heat and electrical conductivity [5]. At last, proton-conducting electrolytes have water production on the opposite side to where the fuel is submitted (cathode) and thus avoiding fuel dilution [6].

The high temperature proton conducting oxides has a lower conductivity compared to oxide ion conductors and because of this the electrolyte thickness in proton conductors has to be in the micron range to reach acceptable PC-SOFC performances[7]. Considering that the global aim is to reach a cell lifetime of 40 000 hours [2, 8] chemical stability and mechanical strength of the thin electrolyte is of crucial importance.

Previous research into SOFC electrolytes has focused mainly on fluorite- and perovskite-type oxides, which are doped with acceptor ions to introduce oxide ion vacancies [9]. Perovskite- type oxides like $BaCeO_3$ and $BaZrO_3$ shows high proton conductivity but suffer from poor chemical and mechanical stability under typical operation conditions [4, 10]. Stability tests clearly demonstrate that $BaCeO_3$ is (i) thermodynamically only slightly stabilized with respect to the binary oxide, (ii) it reacts to carbonate even with small levels of CO_2 and it (iii) form $Ba(OH)_2$ and CeO_2 at high water activities[10]. $BaZrO_3$ on the other hand shows an excellent stability against reaction with CO_2 if compared to $BaCeO_3$. However, $BaZrO_3$ is very refractory which makes it hard to process into dense electrolyte membranes.[2, 11, 12] Rare- earth oxides with fluorite- related structure like $LaNbO_4$ shows high stability in CO_2 and H_2O atmospheres but the oxygen sub lattice in these structures makes the proton conductivity mediocre [4, 13, 14].

Consequently there is a need for new electrode materials with sufficient high temperature proton conductivity and chemical stability toward hydrocarbon derivatives. Lanthanum tungstate has attracted attention due to their relative high proton conductivity. [15] Although La_6WO_{12} is providing to be an interesting candidate as a proton-conducting electrolyte in SOFCs [14], further studies on the stability and appropriate electrode partner materials need to be found to give a firm evaluation of the applicability of these oxides. The aim of this work will therefore be the investigation of chemical stability and compatibility towards other cell components. The chemical compatibility will be tested with two possible cathode materials, $LaCoO_3$ and La_2NiO_4.

2. Literature review

2.1. Background and Previous Work

The lanthunum tungstate structure with a La/W atomic ratio between 4.8 and 6 has been investigated by Magrasó et al. [15] The samples were prepared using the freeze-drying wet-chemical precursor method. The results showed that compounds with a La/W ratio between 5.3 and 5.7 (T=1500°C) obtained single phase. Outside this compositional region, segregation of either La_2O_3 or $La_6W_2O_{15}$ was found. Dense ceramic materials were obtained at 1400 °C. For a La/W ratio of 5.6 the composition was reported to be $La_{6.63}W_{1.17}O_{13.43}$ with calculated density equal to 6.395 g/cm^3 and a lattice size parameter of a= 11.187 Å. The space group were determined to be $F\bar{4}3m$ by XRD and Neutron Powder Diffraction (NPD). [15] However Hage [16] reported that the compound crystallize in a quasi- Fd3m space group by using Convergent Beam Diffraction (CBED). Selected Area Diffraction (SAD) patterns indicated a primitive cubic lattice where the d-glide plain symmetry breaks down. The disagreement in the CBED, SAD and XRD/NPD result might be explained by small structural disorder, but this warrants further investigation. [16]

La_6WO_{12} has been reported to exhibit a relatively high proton conductivity with values in the order of $3\text{-}5\cdot10^{-3}$ S/cm in wet atmosphere under 900°C. At high temperature the materials exhibit n- type electronic conduction under reducing conditions and p- type conduction under oxidizing conditions. [17]

It is reported that the highest conductivity is observed for the undoped La_6WO_{12}.
Aliovalent substitution of Ca^{2+} on a La^{3+} site decrease the relative contribution of ionic conductivity under oxidizing and reducing conditions with increasing concentration of Ca^{2+} doping. At the same time the enthalpy of proton mobility increases, which supports that the decrease in conductivity may be a consequence of trapping of protons, lowering the mobility. [17] The previous work done by Haugsrud [14, 17, 18] has lead to an increasing understanding of how valuable parameters such as oxygen pressure, water pressure and

temperature influences the conductivity. But there are still questions regarding the conductivity decrease upon acceptor doping that needs to be understood.

The author has previously reported the stability and compatibility of the La_6WO_{12} electrolyte with potential oxide cathodes. The potential partner materials $LaCoO_3$ and La_2NiO_4 were investigated via the reaction of fine-grained powders and solid-state diffusion couples. Dense ceramic of La_6WO_{12} were made and coated with the cathode material to form a diffusion couple. These couples were then fired at high temperature. The diffusion-couples cross- section was characterised using scanning electron microscope (SEM) and energy dispersive X-ray spectroscopy spectrometer (EDS). Sample compositions were analysed via element mapping, spot and line scan. To assess phase compatibility, mixtures of micro-fine powders were ground together, pressed into tablet form and fired at high temperature. The reaction products were then analysed via powder X-ray diffraction (XRD). Both studies of $LaCoO_3$ with La_6WO_{12} showed a secondary phase of La_2O_3. In addition a high thermal expansion coefficient gave problems with poor connectivity. In the case of La_2NiO_4 no secondary phases were observed by XRD, but EDS and SEM analysis indicated small amounts of La_2O_3.

The cathode materials $LaMO_3$ (M= Mn, Fe, Co) and La_2NiO_4 have also been investigated with respect to stability and compatibility towards the $LaNbO_4$ electrolyte. The results showed good chemical compatibility for $LaNbO_4$ with the perovskite type compositions ($LaMO_3$), but not with $LaCoO_3$ and the La_2NiO_4 phase. [4]

Previous reactivity studies between La_2NiO_4 and the most widely used SOFC electrolytes, yttria stabilized zirconia (YSZ) and gadolinum-doped cerium oxide (CGO), indicated formation of secondary phases such as Rudden- Popper series $La_{n+1}Ni_nO_{3n+1}$, $LaNiO_3$ and NiO. [19] In the case of $LaCoO_3$ as cathode material, there were several issues regarding the use in YSZ electrolyte cells, including their thermal expansion coefficient and chemical reactivity, which resulted in serve degradation with increasing time of operation. Although doped ceria electrolyte showed less reactivity with $LaCoO_3$ compared with YSZ, the high thermal expansion coefficient remained the main drawback for its use[1].

2.2. Cathodes

Cathodes for solid oxide fuel cells have to possess many properties including high catalytic activity for oxygen molecule dissociation and oxygen reduction, chemical and dimensional stability, high electronic and ionic conductivity, thermal expansion match with other cell components, and compatibility and minimum reactivity with the electrolyte and the interconnector. At last, the cathode must have a stable, porous microstructure that must allow rapid mass transport of reactants and product gases.[1, 8]

The perovskite structures that exhibit mixed ionic and electronic conductivity are very attractive at intermediate temperatures since the polarisation of the cathode increases significantly as the SOFC temperature is lowered. [8] The polarisation makes the mixed ionic-electronic conductors one of the best choices for cathodes because of the extended active areas for oxygen reduction [20]. It is in cells operating around 650 °C that the advantages of using mixed conducting oxides become apparent.

Microstructure and properties of $LaCoO_3$

Lanthanum cobaltites are perovskites with high electrical and ionic conductivities (mixed ionic-electronic conductor). Because of their high conductivities they are used as cathode materials in SOFC, oxygen permeable membranes, and are active catalyst for oxidation of CO. Pure $LaCoO_3$ has a rhombohedral structure at room temperature and remains rhombohedral up to temperatures close to the melting point.[21] However, the rhombohedral distortion from cubic symmetry is linearly decreasing with increasing temperature [22]. A figure displaying the structure of a standard cubic perovskite is presented in Figure 2.1.

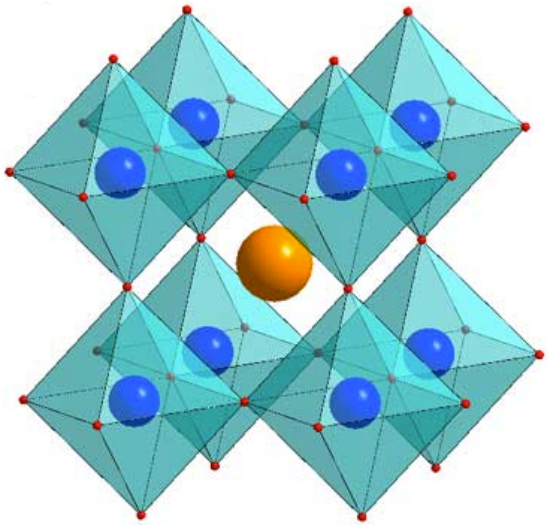

Figure 2.1 Standard cubic perovskite [23].

$LaCoO_3$ is known to be unstable in reducing atmospheres. When $LaCoO_3$ is present as a powder, where surface reaction will prevail, the reduction starts at a low temperature with formation of metallic Co and La_2O_3 at 600 °C. In the bulk form, $LaCoO_3$ undergoes a series of expansions and contractions due to phase transformations.

Under oxidizing conditions a significant increase of the thermal expansion coefficient (TEC) occurs both during heating and cooling. $LaCoO_3$`s high thermal expansion as well as structural, mechanical and phase instability limits the use of $LaCoO_3$ in applications such as fuel cells, oxygen permeable membranes and sensors. [24]

Microstructure and properties of La_2NiO_4

The crystal structure of the Ruddlesden-Popper type phase La_2NiO_4, is described as stacked perovskite ($LaNiO_3$) layers alternating with rock-salt (La_2O_3) layers along the c direction [20]. It has a high-temperature tetragonal phase (T>680 K) a low temperature orthorhombic phase, and a low-temperature tetragonal phase (T<70 K) [25]. A figure displaying the structure of a stacked perovskite is presented in Figure 2.2.

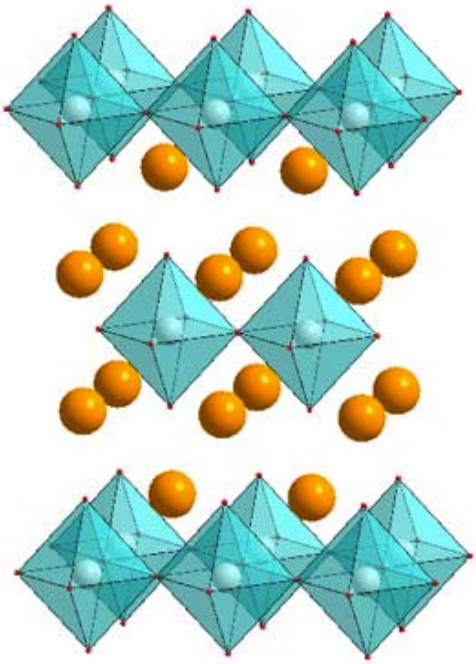

Figure 2.2 Ruddleson- Popper phase [23]

La_2NiO_4 shows mixed ionic- electronic conduction and is a good candidate for inter-mediate temperature electrodes [26]. In addition, the La_2NiO_4 phase has a significantly lower thermal expansion coefficient than the cobaltite's that are commonly used in inter-mediate temperature electrolytes. Though La_2NiO_4 shows high oxygen bulk diffusion and surface exchange coefficient, its lower electronic conductivity limits the practical use as SOFC cathode. The electronic conductivity can however be improved by doping to produce extra charge carriers.[20]

2.3. Solid- state diffusion couple

In a diffusion couple, two materials of different composition are joined together and subsequently held for a certain time at an elevated temperature. Diffusion couples are widely used to study interdiffusion phenomena and to determine isothermal phase diagram sections. [27] The understanding of interdiffusion in solids are important in material science since diffusion processes are appearing in solid matter at elevated temperatures. Diffusion plays a key role in the kinetics of many micro structural changes that occur during heat treatment of different materials. Typical examples of such changes are nucleation of new phases, diffusive phase transformations, precipitation and dissolution of a second phase, recrystallization, high-temperature creep, and thermal oxidation. The knowledge of interdiffusion between materials used in technological applications like SOFCs is crucial when choosing the proper partner materials.[28]

2.4. Solid- state diffusion

In pure materials containing vacancies, atoms move or "jump" from one lattice position to another. This process is known as self-diffusion, and can be detected by using radioactive tracers. Although self-diffusion occurs continually in all materials, its effect on the materials behaviour is not significant. [29]

Diffusion of unlike atoms in different directions is known as interdiffusion. If the sample are held at an elevated temperature one will expect the atoms to diffuse from the high concentration side to the to the low concentration side. The rate at which atoms diffuse in a material can be measured by the flux J. At steady- state conditions Ficks first law explains the flux of atoms:

$$J_i = -D_i \frac{dc_i}{dx} \tag{2.1}$$

where J_i is the flux of atoms of type i, D_i is the diffusion coefficient of atom of type i, c_i is the concentration of atoms i and dx is the position in the solid.[29]

In practice, the steady-state conditions cannot often be established during experiments due to for example time constrains. A material balance in the volume element of the system then becomes useful. The following expression in one-dimension can be derived from Figure 2.3.[30]

$$\partial C \partial x = (Flux \;\; in - Flux \;\; out)\partial t$$
$$\frac{\partial C}{\partial t} = D\frac{\partial^2 C}{\partial x^2} \qquad (2.2)$$

The solution to this equation depends on the boundary conditions for a particular situation[29, 30].

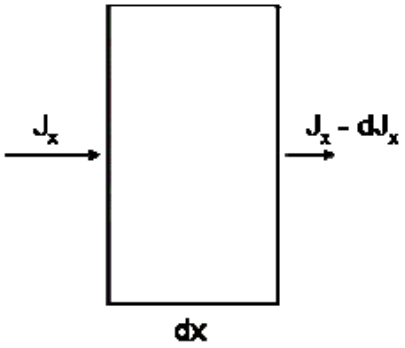

Figure 2.3 One-dimensional mass balance in an infinitesimal system[30]

Atoms can diffuse through the material via several mechanisms. All types of substitutional diffusion have been shown to operate through a *vacancy mechanism.* In this type of mechanism, an atom leaves its lattice site to fill a nearby vacancy. However vacancies is not required for diffusion to happen. When a small interstitial atom is present in the host material, the atom can move from one interstitial site to another. This type of diffusion mechanism is called *interstitial diffusion*. A third mechanism, *interstitalcy diffusion,* is considered to be a combination of the substitutional and interstitial mechanism. The principle of the interstitialcy mechanism is that an interstitial atom displaces another atom from its original substitutional site into an adjacent position. The different mechanisms are summarized in Figure 2.4.

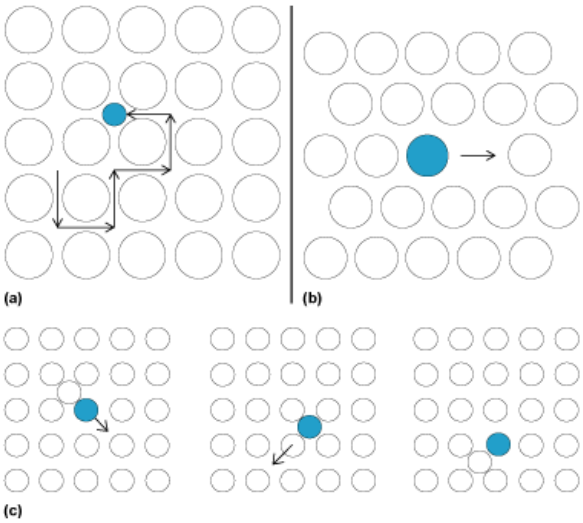

Figure 2.4 Diffusion mechanisms: (a) interstitial; (b) vacancy; (c) interstitialcy [28]

Thermal energy associated with atoms, ions etc. cause the random movement of atoms as illustrated above. At a microscopic scale the thermodynamic driving force for diffusion is concentration gradient. If two different materials A and B are opposed to each other a net or an observable flux is created, which depend on the temperature and concentration gradient.[29] The concentration gradient shows how the composition of the material varies with distance. An illustration of the concentration profile when two different materials, A and B, are placed in contact is given in Figure 2.5.

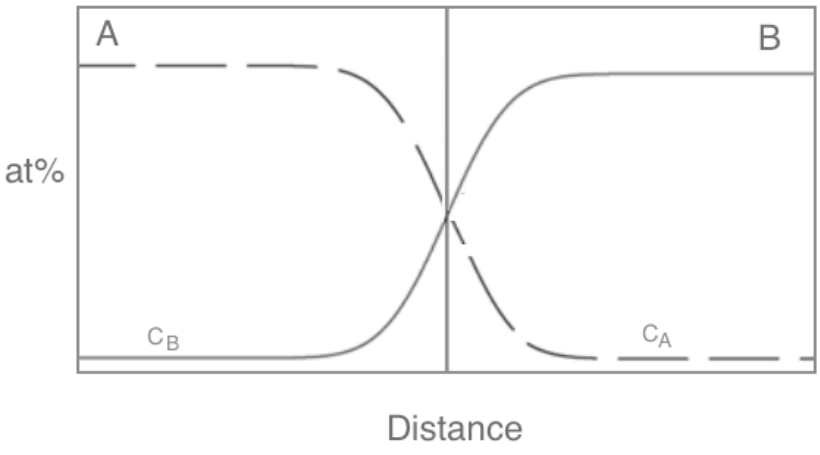

Figure 2.5 Illustration of interdiffusion concentration profile between component A and B.

2.5. Solid- state reaction

If a reaction between the two different materials A and B does not occur an interdiffusion will take place as described above. If these materials do react, a third and, possibly, also forth and fifth phases are formed on the interface between the reactants. [30]

Kirkendall effect

Consider the diffusion couple illustrated in Figure 2.6 between A and B, where the diffusion rates of the two species are different ($D_B > D_A$). Since the diffusion fluxes are different, the original interface (Kirkendall plane) between the materials moves during the experiment[30]. This can only happen if diffusion is by vacancy mechanism[31]. In order to track the position of the initial interface it is therefore necessary to place inert markers between the materials before heat treatment. The movement of the marker, v_K, is a function of the individual chemical diffusion coefficients and is given by the Kirkendall equation

$$v_K = (D_A - D_B)\frac{\partial X_A}{\partial x} \tag{2.3}$$

where $\frac{\partial X_A}{\partial x}$ is the concentration gradient at the Kirkendall plane.[30]

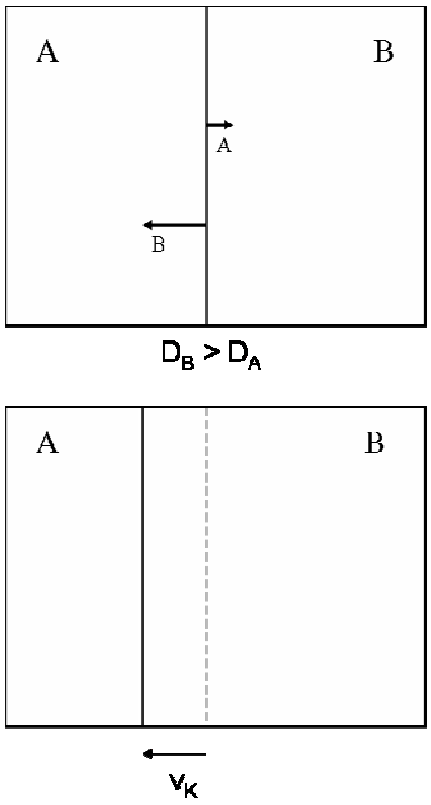

Figure 2.6 Illustration of the Kirkendall effect[30]

Diffusion kinetics and the parabolic rate law

The growth kinetics of a single compound layer is determined by a combination of two types of processes, namely by (i) the *diffusion* of matter across the compound layer where the diffusion flux slows down with increasing layer thickness, and by (ii) the *rearrangement* of the atoms at the interfaces required for growth of the compound layer which may involve a reaction barrier[32]. If the diffusion process is rate limiting and controls the growth, the corresponding kinetics is termed diffusion controlled and the layer thickness increases proportional to the square root of time *t*. This type of kinetics is also known as parabolic. If the interfacial reaction barriers control the kinetics, it is termed interface controlled (or boundary or reaction controlled) and the thickness increase linearly with time. The two processes are illustrated graphically in Figure 2.7. Further, only the parabolic rate law will be discussed.

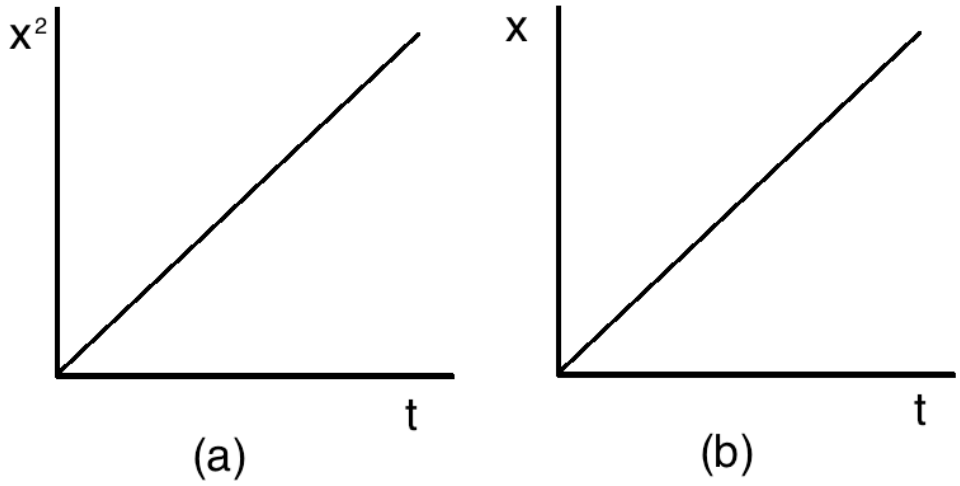

Figure 2.7 Layer thickness as a function of time (a) diffusion controlled; (b) interface controlled.

The rate at which the total layer thickness grows is controlled by the speed of the slowest diffusing specie. If the layer increases by an amount Δx in a period of time Δt, the rate of film growth, d(Δx)/d(Δt), is given by

$$\frac{d(\Delta x)}{d(\Delta t)} = \frac{k_p}{x} \tag{2.4}$$

where k_p is the parabolic rate constant and x is the film thickness at time t. Integration an rearrangement of this equation leads to the following expression

$$x^2 = 2k_p t + C \tag{2.5}$$

where C is an integration constant.[30, 33]

The analysis of solid-state reaction kinetics between oxides is a very complex process since the number of possible mobile components and correspondingly, the number of possible reaction mechanisms increase dramatically[30]. The reader is referred to the work done by I.V. Dybkov [34] for a more detailed presentation of reaction diffusion and solid state chemical kinetics.

3. Experimental

3.1. Materials preparation

Powders of $LaCoO_3$ and La_2NiO_4 were prepared via spray pyrolysis as reported elsewhere [4]. The powders were then calcined in air at 1100 °C for 7 hours to remove remaining nitrates/organics. Powder of La_6WO_{12} with a La/W atomic ratio of 5.6 (LWO56) was prepared via spray pyrolysis and calcined at 800 °C by CerpoTech company.

Dense LWO56 ceramics were produced via uniaxial pressing followed by firing at 1400 °C for 2 h in air with heating and cooling rates of 200 °C/h. Dense $LaCoO_3$ and La_2NiO_4 pellets were produced by firing at 1350 °C for 6 h in air with heating an cooling rates of 200 °C/h. The sintered pellets were then prepared for polishing by embedding them in epoxy resin (EpoFix) to facilitate their handling and to improve the preparation results. The epoxy hardened for minimum 15 hours before the pellets were polished with fine abrasives down to 1 μm. The epoxy was afterwards removed by immersing the specimen in chloroform and let it react until all of the epoxy was dissolved.

To study the interdiffusion between LWO56 and $LaCoO_3$/La_2NiO_4, solid-state diffusion couples were made. The couples were formed by facing the polished surfaces of LWO and cathode materials between alumina disks as illustrated in Figure 3.1.

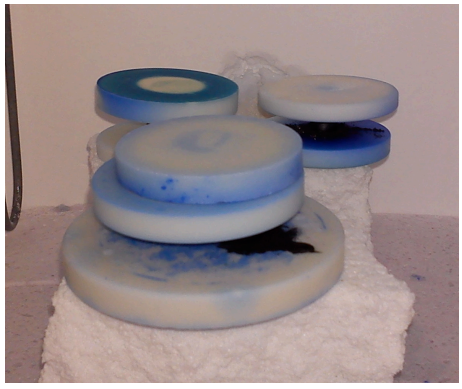

Figure 3.1 Furnace setup. Diffusion couples pressed between alumina disks.

Three thin lines of platinum paint were drawn on one of the policed surfaces in the diffusion couple to mark the initial interface. Powder of the reactants was used between the diffusion couples surface and alumina disks to avoid reaction (not for the diffusion couple fired at 50 hours). The diffusion couples were then heat treated at 1450 °C at 20, 50 and 100 hours. Heating rates were 120 °C/h up to 500 °C where the temperature was held for 1 h to burn of remaining nitrates/organics from the platinum paint. Heating rates above 500 °C and cooling rates were 200°C/h.

After each heat treatment the couples were mounted in epoxy resin and cut with a diamond saw perpendicular to the reaction surface. The cross- section was then polished with fine abrasives down to 1 μm and coated with carbon.

3.2. Characterization

Determination of bulk density, open porosity and total porosity of dense pellets was measured by Archimedes method [35] using isopropanol as immersion liquid. Table 3.1 gives the crystallographic densities that was used in the calculations.

Table 3.1 Crystallographic densities for the sintered materials.

Composition	Crystallographic density [g/cm^3]
La_6WO_{12} (LWO56) [15]	6.395
$LaCoO_3$ [36]*	7,197
La_2NiO_4 [37]*	7,070

* Crystallographic density given in the X-ray PDF database

Scanning electron microscope (SEM, Hitachi S-3400N) was used to study the polished- and unpolished surface of the dense pellets. The grain size of the unpolished surface was found by the linear intercept method [38].

The microstructure of the diffusion couples were characterised by scanning electron microscopy (SEM, Hitachi S-3400N) equipped with an Oxford Instruments INCA X-sight (model 7021) energy dispersive X-ray spectroscopy (EDS) spectrometer. All analysis was performed using the Oxford Instruments INCA analysis tool.

4. Results

4.1. Densification and microstructure

Dense pellets of LWO56 was obtained by sintering for 2 hours at 1400°C in air while dense pellets of $LaCoO_3$ and La_2NiO_4 was obtained by sintering for 6 hours at 1350°C. Average values for bulk density (ρ_b), open porosity (π_a), closed porosity (π_f) and total porosity (π_t) are given in Table 4.1.

Table 4.1 Average values for bulk density (ρ_b), open porosity (π_a), closed porosity (π_f) and total porosity (π_t) measured with Archimedes method using isopropanol as immersion liquid.

Sample	ρ_b [g/cm^3]	π_a [%]	π_f [%]	π_t [%]	Density [%]
LWO56	6,09	4,59	0,23	4,81	95,19
$LaCoO_3$	6,78	0,44	5,34	5,78	94,22
La_2NiO_4	6,88	0,82	1,80	2,62	97,38

Microstructures of the sintered samples are shown in Figure 4.1 and Figure 4.2. The average grain size of LWO56, $LaCoO_3$ and La_2NiO_4 is found by the linear intercept method and is 3,00 µm, 19,09 µm and 4,93 µm respectively. Pores are observed along grain boundaries as well as inside grains for all sintered pellets.

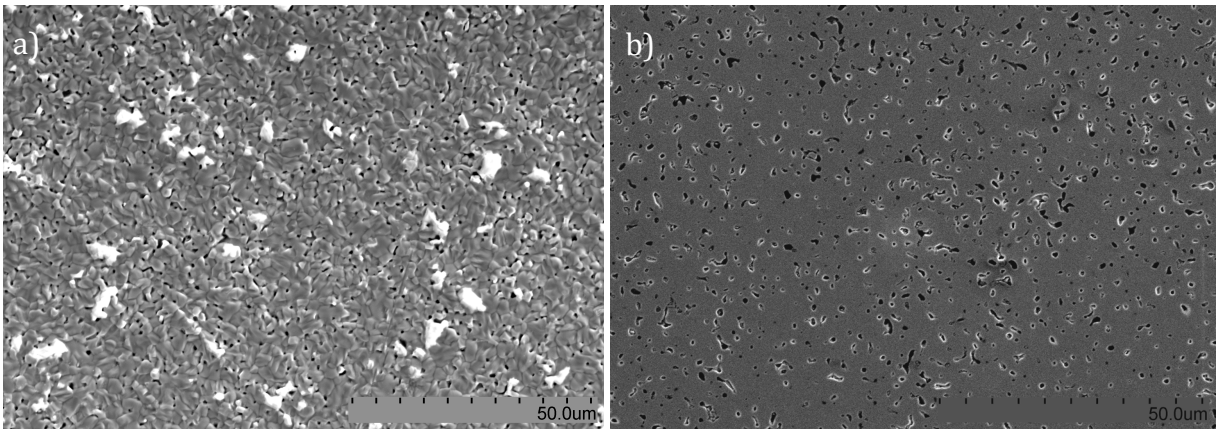

Figure 4.1 Microstructure of LWO56 pellet sintered at 1400 °C for 2 h. (a) Unpolished surface and (b) polished surface

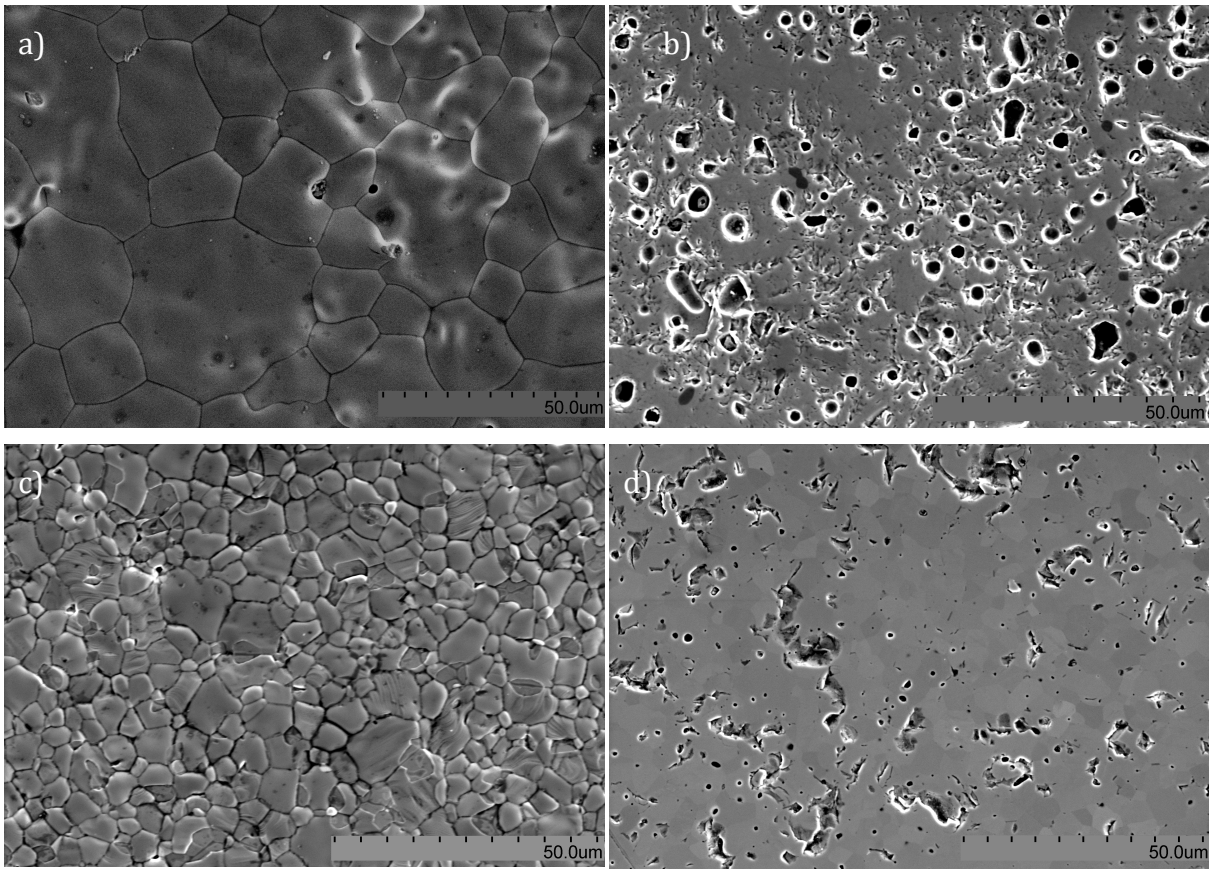

Figure 4.2 Microstructure of cathode materials sintered at 1350 °C for 6 h. (a) Unpolished surface of $LaCoO_3$, (b) polished surface of $LaCoO_3$, (c) unpolished surface of La_2NiO_4 and (d) polished surface of La_2NiO_4.

4.2. LWO56 – $LaCoO_3$ diffusion couples

Typical cross sectional views of diffusion couples are shown in Figure 4.3 and Figure 4.4. A product layer of $LaCo_{1-x}W_xO_3$ is evident between the two reactants. The thickness of the product layer depends on the diffusion length of the active species and hence the dwell time. Precipitates of this phase were also found in the LWO56 bulk phase. The precipitate distribution was random and could be found throughout the bulk. Due to thermal mismatch of the materials the diffusion couples fractured along the $LaCo_{1-x}W_xO_3$/LWO interface. Since the diffusion couples were mounted in epoxy resin after the reaction, a black layer separate the phases, but in less degree in the 50- hour diffusion couple (Figure 4.3).

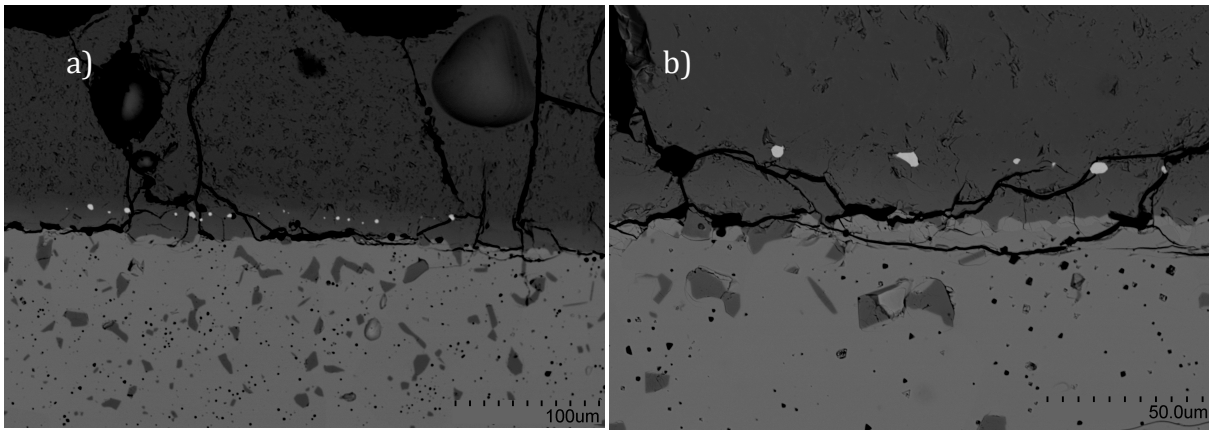

Figure 4.3 Backscattered electron micrograms of diffusion couple after 50 h firing at 1450 °C in air. Phases from the top: $LaCoO_3$, $LaCo_{1-x}W_xO_3$, LWO56

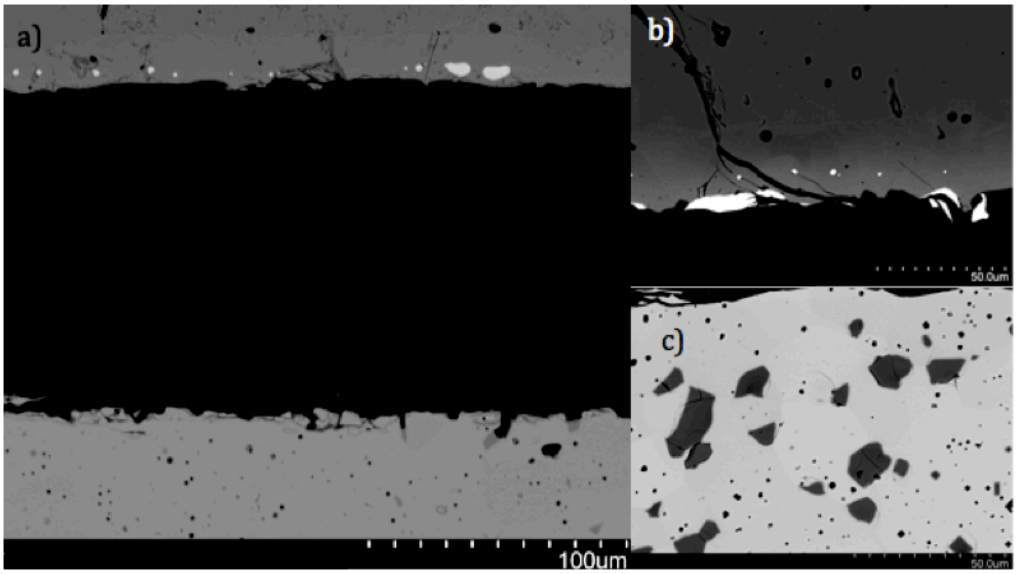

Figure 4.4 Cross sectional view of the diffusion couple fired for (a) 20 h and (b,c) 100 h

EDS analysis were used to investigate the chemical composition across the diffusion couple. Line scans are given in Figure 4.5 to Figure 4.7. Two separate line scans are given for the diffusion couple with 20- and 100-hour dwell time due to large separations between the phases. For the diffusion couple with 50- hour dwell time the measurements started in the bulk of $LaCoO_3$, continued across the interface and ended in the LWO56 phase.

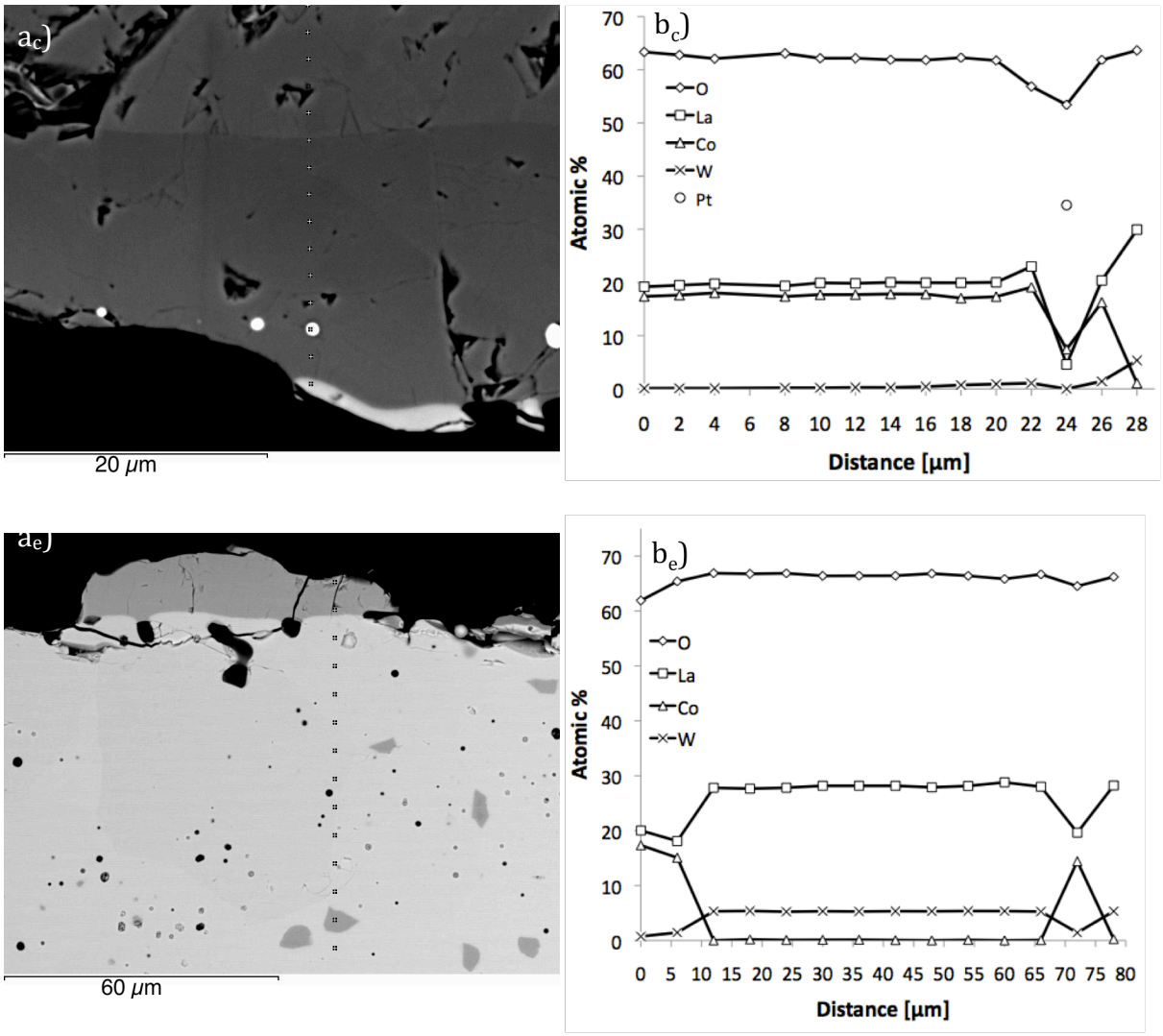

Figure 4.5 (a) Backscattered electron micrographs of the LWO56/$LaCoO_3$ diffusion couple fired for 1450°C in air, a_c cathode micrograph and a_e electrolyte micrograph. (b) Phase composition taken along the line profiles shown in (a).

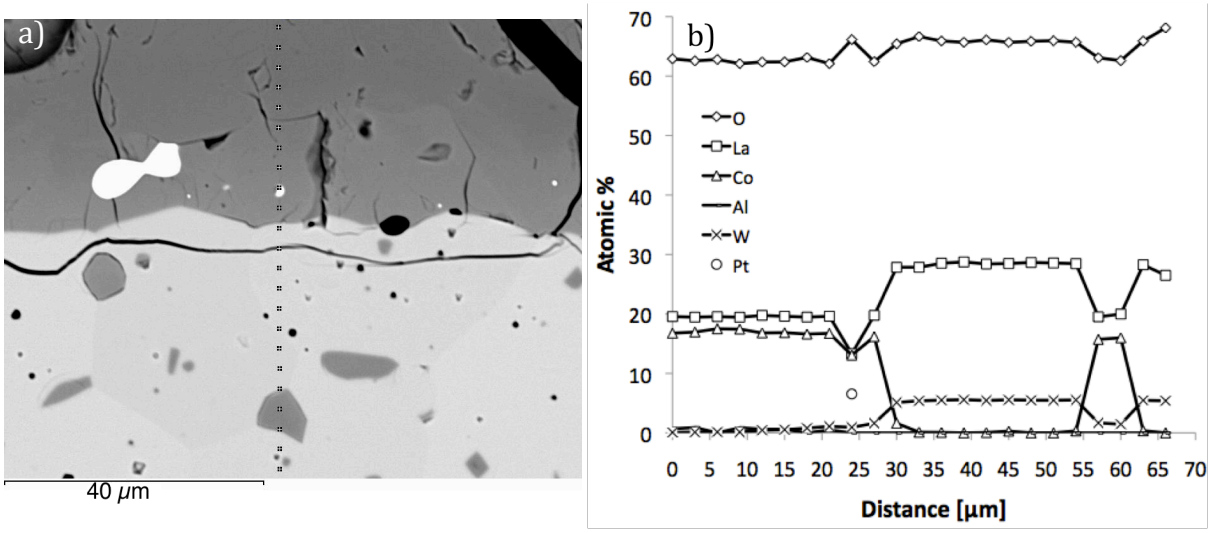

Figure 4.6 (a) Backscattered electron micrograph of the LWO56/$LaCoO_3$ diffusion couple following 50 hour firing at 1450°C in air. (b) Phase composition taken along the line profile in (a).

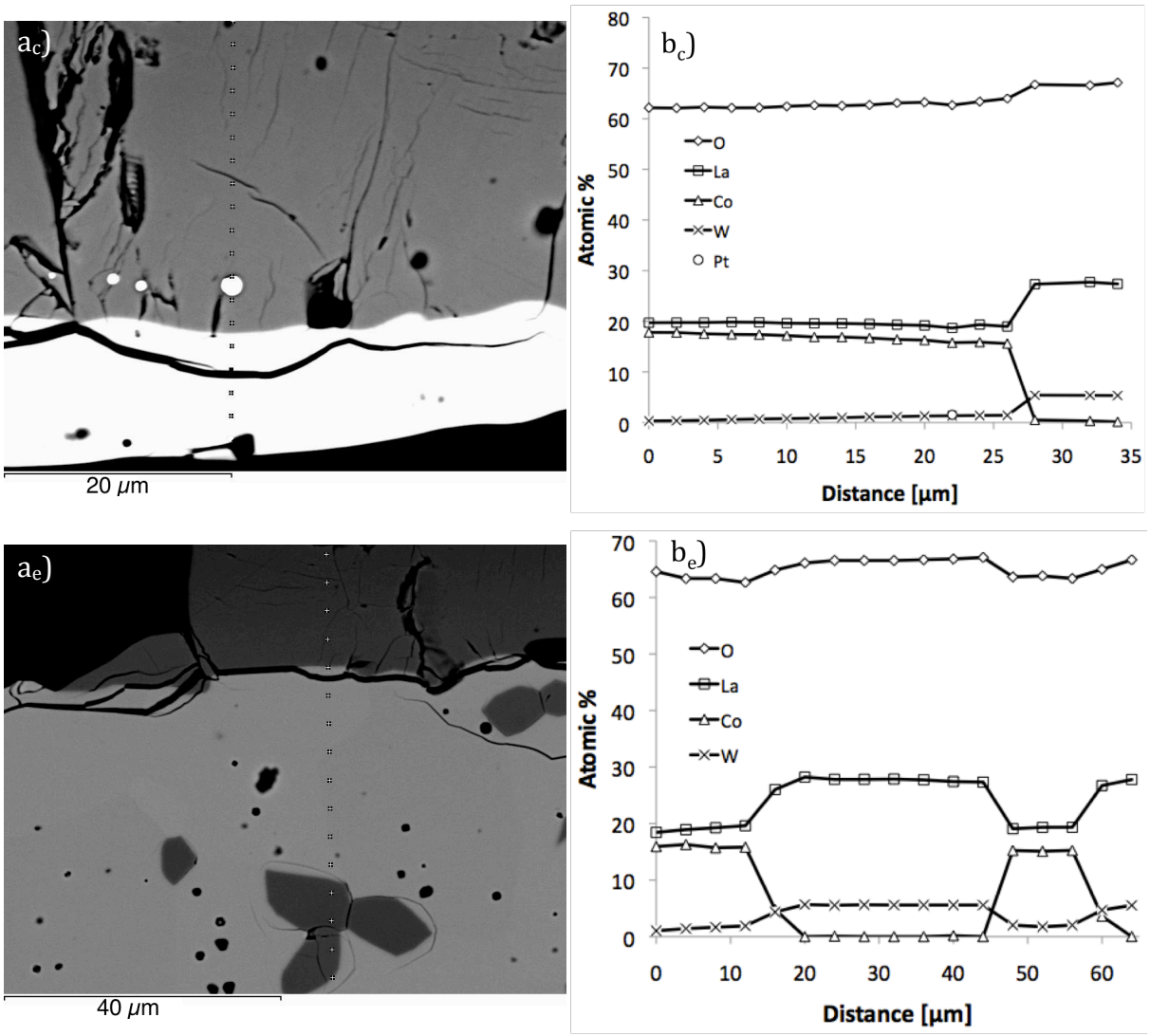

Figure 4.7 (a) Backscattered electron micrographs of the LWO56/$LaCoO_3$ diffusion couple fired for 1450°C in air, a_c cathode micrograph and a_e electrolyte micrograph. (b) Phase composition taken along the line profiles shown in (a).

The diffusion couples of the LWO56-$LaCoO_3$ system shows evidence of diffusion of cobalt into the electrolyte and diffusion of tungsten into the cathode. The highest content of tungsten in the $LaCo_{1-x}W_xO_3$ phase was found below the platinum markers, and x is increasing with increasing dwell time in the range of 0,07 to 0,1. Above the platinum markers the tungsten content gradually decrease with increasing length from the initial interface. The tungsten content in the precipitates is found to be the same as in the product phase below the platinum markers.

Small amounts of cobalt were detected in the bulk of LWO56, whereas larger amounts were found in precipitations. In the precipitates the Co/La ratio is 0,05 - 0,1 lower than

the measured Co/La ratio in the $LaCoO_3$ phase, which proves that tungsten substitutes 5-10 percent of the cobalt content in the $LaCo_{1-x}W_xO_3$ phase.

X-ray element mappings of the diffusion couple fired for 50 hours are presented in Figure 4.8. The element map of cobalt clearly states the high content of cobalt in the precipitates and the product layer. There is no evidence of a diffusion gradient below the product layer. The tungsten element map confirms the line scan results that indicated a concentration gradient above the initial LWO56/$LaCoO_3$ interface. The tungsten content seems rather uniform below the initial interface, and gradually decreases above the Pt-markers. From this map the $LaCo_{1-x}W_xO_3$ precipitates appear to have the same content of tungsten as the product phase at the interface.

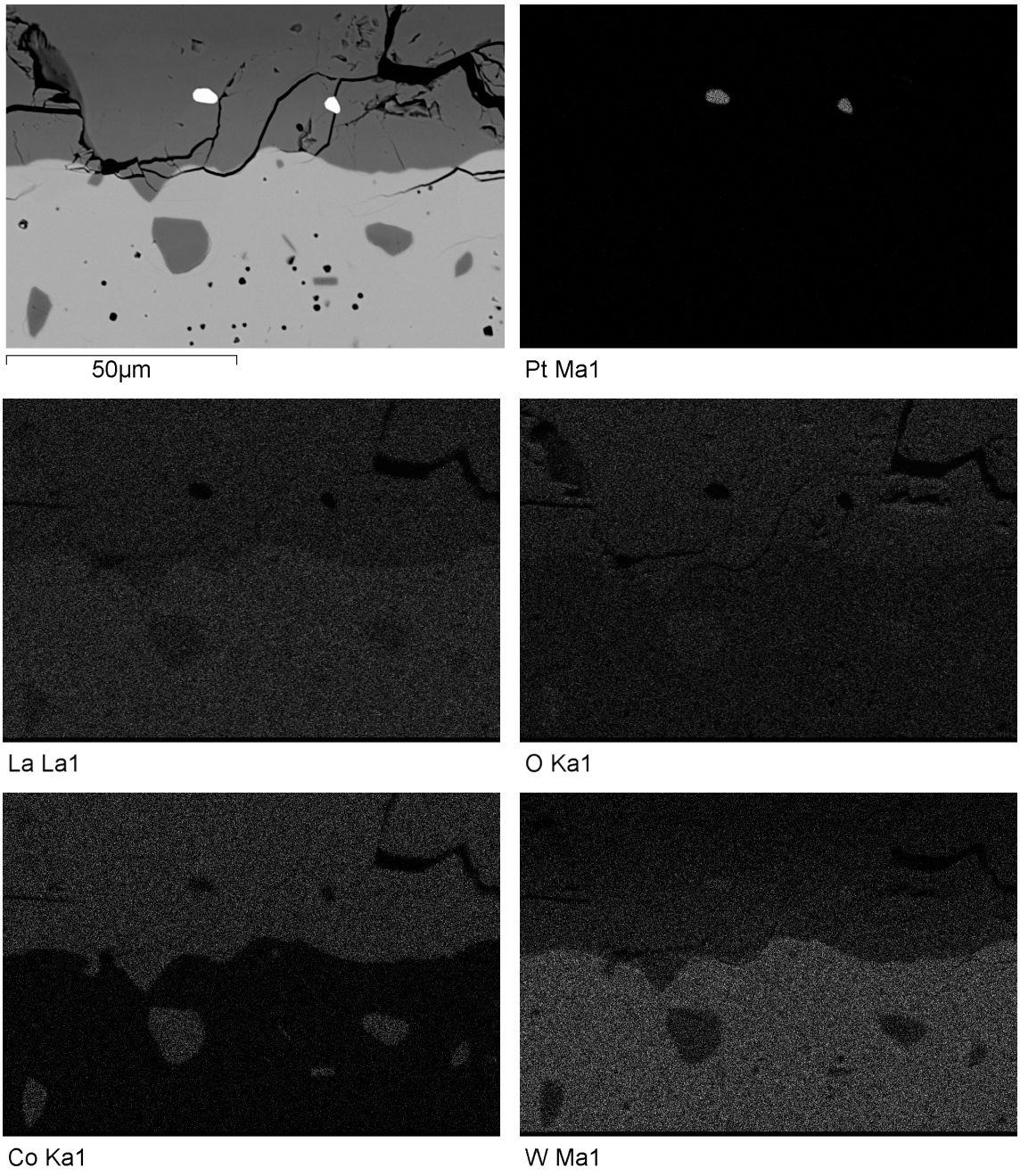

Figure 4.8 Element mappings of the diffusion couple fired for 50 hours at 1450°C. Maps are given for the elements: Pt, La, O, Co and W

Growth kinetics

Growth kinetics of the $LaCo_{1-x}W_xO_3$ layer below the platinum markers is illustrated in Figure 4.9. The thickness of the product, x, is measured from 6-15 different vertical positions in the sample. Up to 50 hours there is a linear trend and the measured thickness, x, follows the parabolic rate law. After 100 hours de measured thickness is as low as the measured thickness after 20 hours.

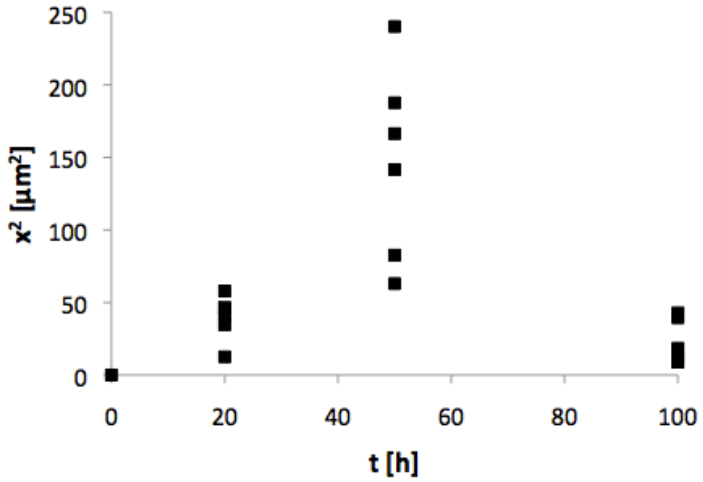

Figure 4.9 Plot of product layer thickness versus dwell time at 1450 °C in air.

Precipitates in the LWO phase

Figure 4.10 shows $LaCo_{1-x}W_xO_3$ as a precipitated phase in LWO. The precipitates where found throughout the bulk, and the content and size increase with increasing dwell time.

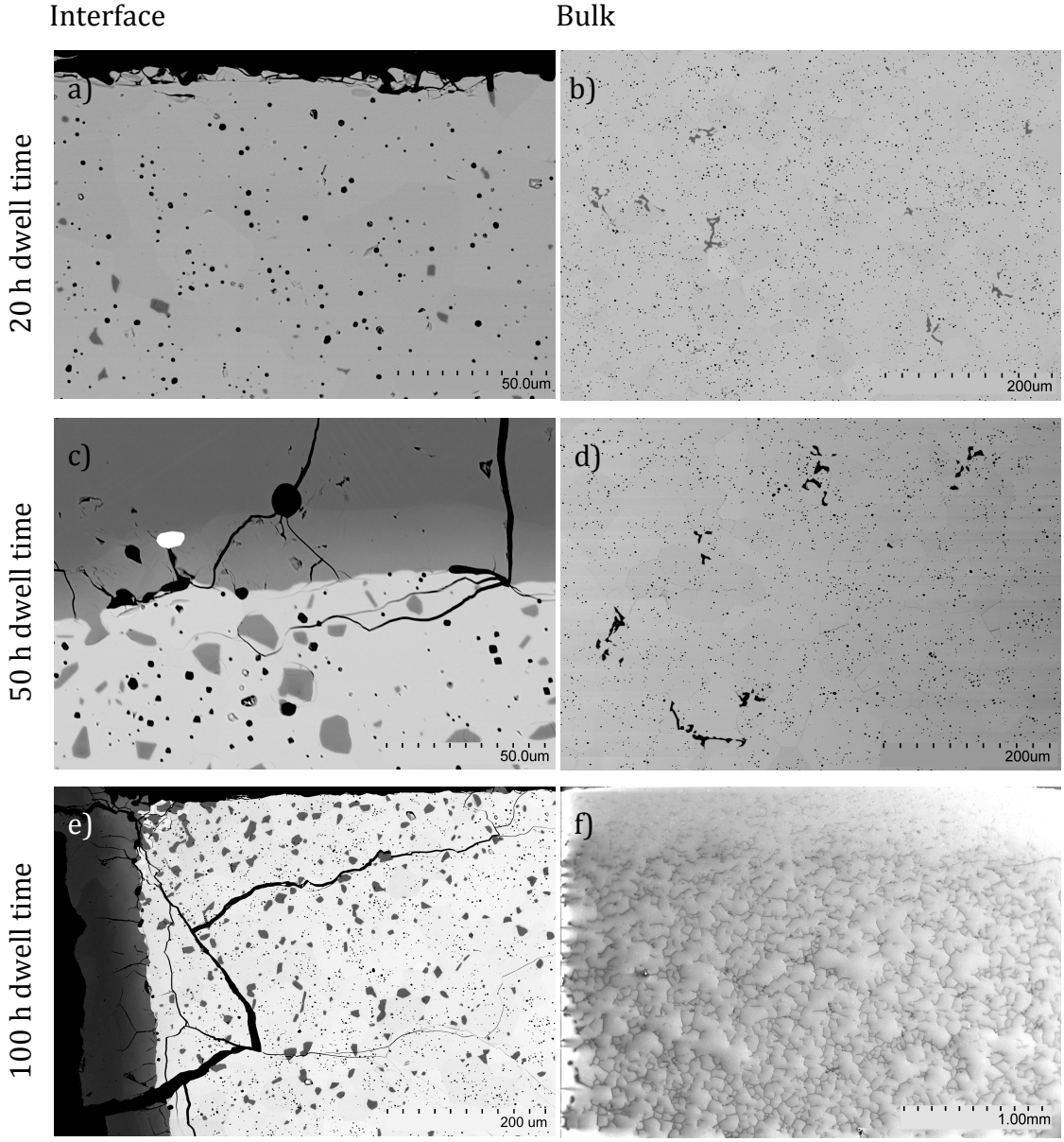

Figure 4.10 Backscattered electron micrograph of precipitates following 20, 50 and 100 h firing at 1450 °C in air.

EDS analysis of a single precipitation close to the interface is given in Figure 4.11.

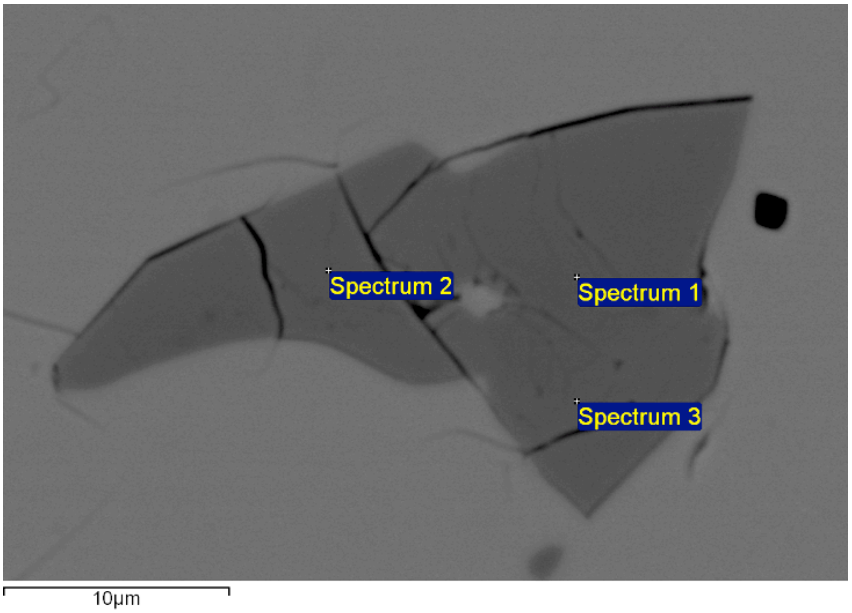

Spectrum	O [at%]	Co [at%]	La [at%]	W [at%]
1	62,64	15,91	19,74	1,71
2	62,68	15,58	19,77	1,97
3	61,08	16,90	20,28	1,74

Figure 4.11 EDS analysis of precipitation close to the interface after 50 h firing at 1450 °C. All results are given in atomic percent.

The precipitates in the middle of the LWO bulk contain a lot of impurities. The impurities seems to be gathered as inclusions inside the $LaCo_{1-x}W_xO_3$ precipitate and can be seen as a darker phase. EDS analysis of precipitates in the middle of the LWO bulk are given in Figure 4.12.

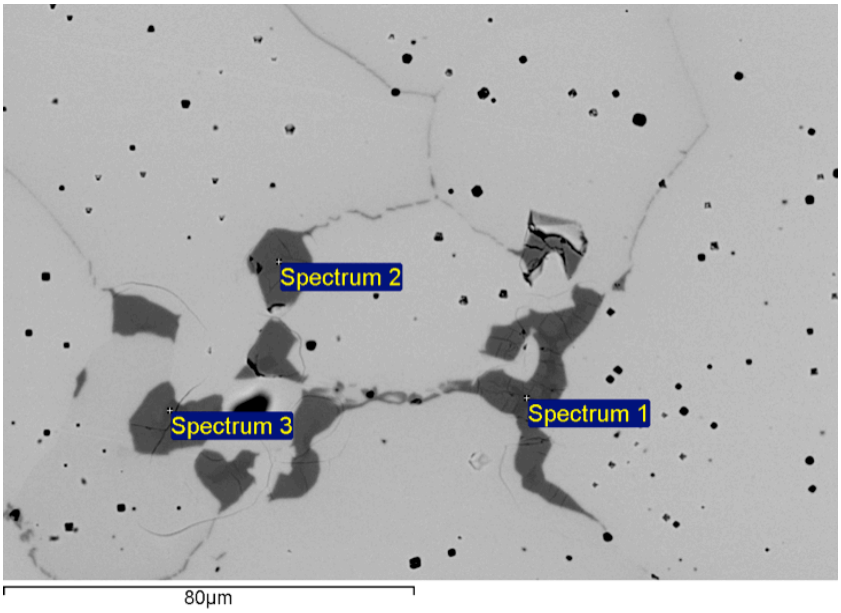

Spectrum	O [at%]	Al [at%]	Mn [at%]	Fe [at%]	Co [at%]	La [at%]	W [at%]
1	63,24	0,84	5,94	1,88	8,29	19,40	0,41
2	63,04	0,62	3,95	1,69	10,46	19,51	0,73
3	62,87	0,62	5,93	2,23	8,36	19,53	0,46

Figure 4.12 EDS analysis of precipitations in the middle of the LWO bulk after 100 h firing at 1450 °C. All results are given in atomic percent.

Diffusion and reaction on the $LaCoO_3$ /Al_2O_3 interface

In the first heat treatment of the $LaCoO_3$/LWO diffusion couple (50 h) no powder bed were used between the diffusion couples and alumina disk. The line scan result from this diffusion couple indicated small amounts of Al in the $LaCoO_3$ phase close to the initial interface (Figure 4.6). In addition the look of the sample in Figure 4.13 indicate that $LaCoO_3$ has been plastically deformed during heating. The load was therefore halved for the next experiments.

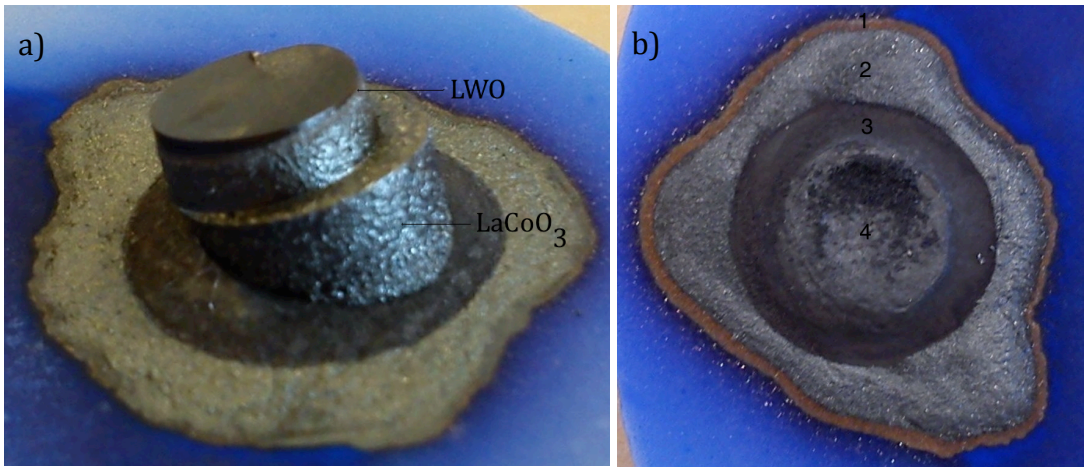

Figure 4.13 (a) $LaCoO_3$/LWO diffusion couple after 50 h firing at 1450 °C in air. (b) Part in (a) that were analysed by EDS.

The reaction product at the $LaCoO_3$/Al_2O_3 interface were analysed by EDS. Chemical compositions from the marked areas in Figure 4.13 (b) are given in Figure 4.14. The results indicate formation of $LaAlO_3$ and CoO.

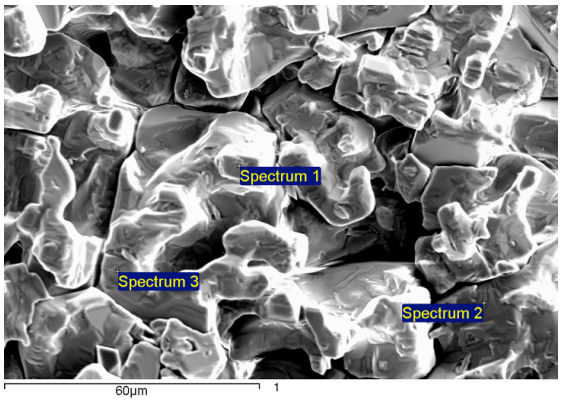

Spectrum	O [at%]	Al [at%]	Co [at%]	La [at%]
1	50,81	16,69	0,83	31,67
2	65,33	17,39	0,28	16,99
3	62,92	17,60	0,34	19,13

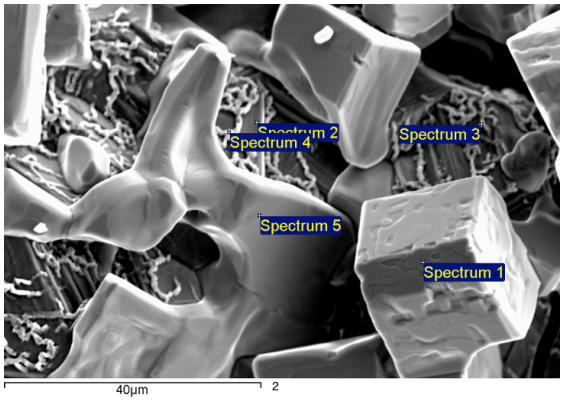

Spectrum	O [at%]	Al [at%]	Co [at%]	La [at%]
1	62,15	16,33	1,65	19,56
2	66,45	0,36	32,50	0,68
3	67,04	0,60	31,38	0,98
4	50,64	0,76	46,92	1,68
5	51,01	15,17	2,55	31,27

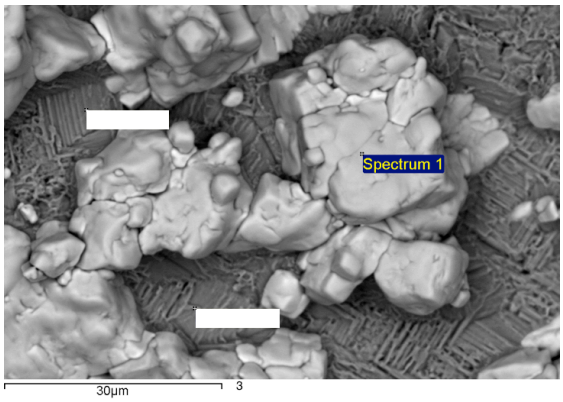

Spectrum	O [at%]	Al [at%]	Co [at%]	La [at%]
1	66,63	12,89	3,92	16,30

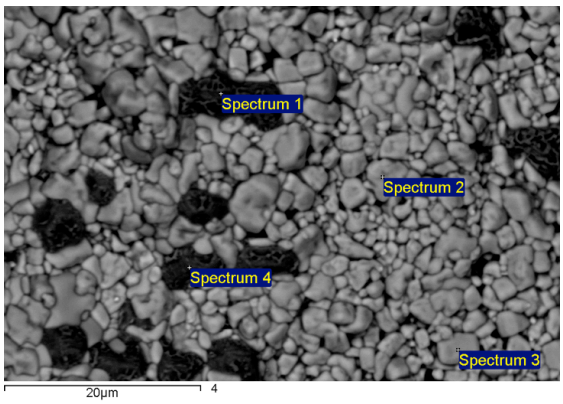

Spectrum	O [at%]	Al [at%]	Co [at%]	La [at%]
1	57,55		41,92	0,53
2	57,89	11,38	7,48	23,26
3	62,13	12,24	5,74	19,89
4	43,47	0,75	54,60	1,18

Figure 4.14 EDS analysis of reaction products at the $LaCoO_3/Al_2O_3$ interface. Electron images 1-4 correspond to those areas marked in Figure 4.13 (b).

4.3. LWO56 – La_2NiO_4 diffusion couples

Typical cross sectional views of diffusion couples are shown in Figure 4.15 and Figure 4.16. A composite product layer of La_2O_3 and LWO is evident between the two reactants. The darker needle shaped product is La_2O_3 and smaller amounts of LWO are found in between the needle's. LWO is also found as randomly distributed precipitates in the La_2NiO_4 phase *close* to the interface. The precipitates located near the interface are more rounded than the precipitates in the bulk, which has a needle shaped form. EDS analysis indicates that the precipitates in the bulk are La_2O_3. The diffusion couples fired for 20 and 100 hours (Figure 4.16) fractured along the initial interfaces.

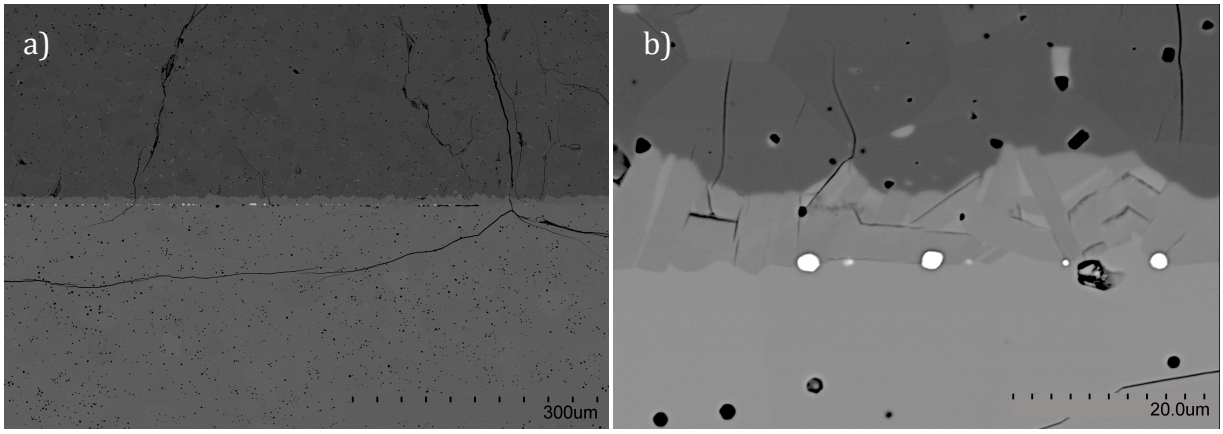

Figure 4.15 Backscattered electron micrograms of diffusion couple after 50 h firing at 1450 °C in air. Phases from the top: La_2NiO_4, La_2O_3 / LWO composite, LWO56

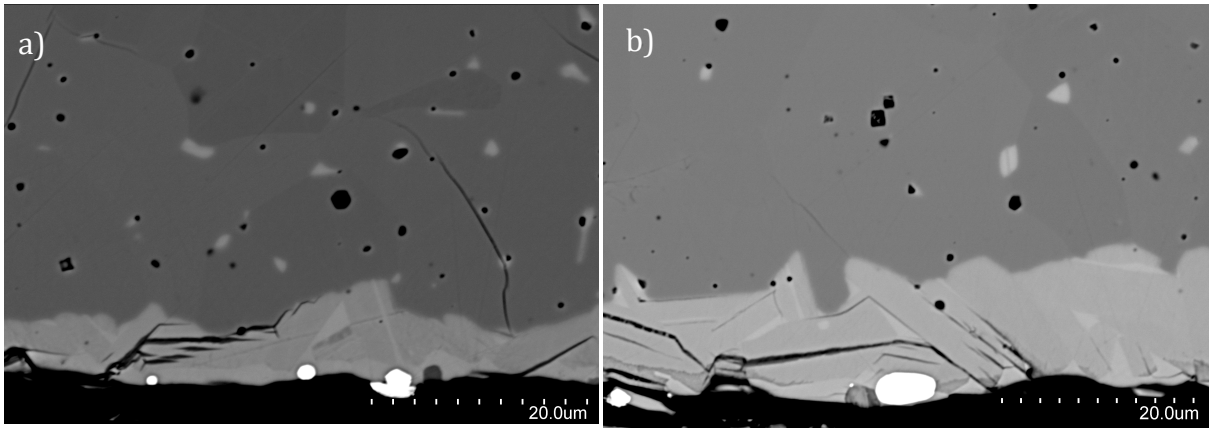

Figure 4.16 Backscattered electron micrograms of diffusion couple after firing at 1450 °C in air for (a) 20 h and (b) 100 h. Phases from the top: La_2NiO_4, La_2O_3/LWO composite, epoxy (black phase).

EDS analysis were used to investigate the chemical composition of the diffusion couple. Line scans measured across the diffusion couples are given in Figure 4.17 and Figure 4.18.

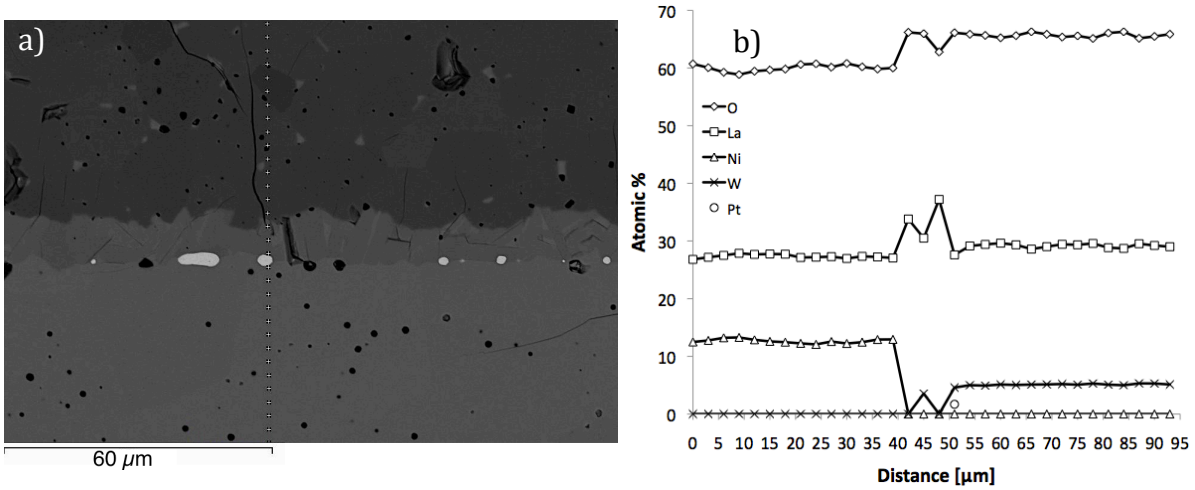

Figure 4.17 (a) Backscattered electron micrograph of the LWO56/La_2NiO_4 diffusion couple after 50 hour firing at 1450°C in air. (b) Phase composition taken along the marked line in (a).

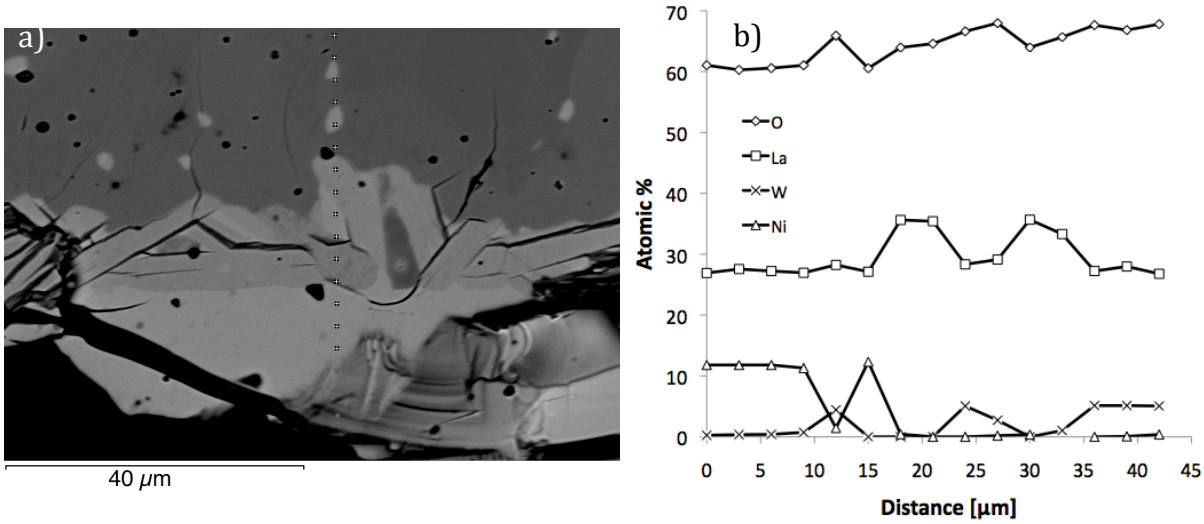

Figure 4.18 (a) Backscattered electron micrograph of the LWO56/La_2NiO_4 diffusion couple after 100 hour firing at 1450°C in air. (b) Phase composition taken along the marked line in (a).

There is no evidence of diffusion of nickel between the phases in the diffusion couple fired for 50 hours (Figure 4.17). Tungsten was found in the product layer, and point scan measurements indicate precipitations of LWO in the La_2NiO_4 phase. The results from the

line scan measurement did not indicate any tungsten outside these precipitates. In the diffusion couple fired for 100 hours (Figure 4.18) small amounts of nickel were found in the LWO phase and small amounts of tungsten in the La_2NiO_4 phase. Larger amounts of tungsten were found in the precipitates and product layer.

Point scan measurements of the product layer and precipitate are given in Figure 4.19.

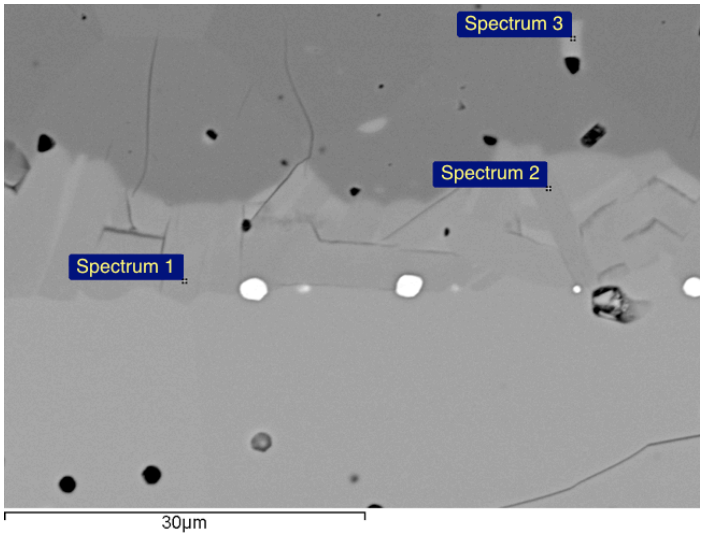

Spectrum	O [at%]	Ni [at%]	La [at%]	W [at%]
1	62,40	-	37,60	-
2	62,43	-	37,57	-
3	65,34	0,63	29,15	4,89

Figure 4.19 EDS point scan analysis of product layer (spectrum 1 and 2) and LWO precipitate (spectrum 3) of the diffusion couple fired for 50 h. Phases from the top: La_2NiO_4, La_2O_3/LWO composite, LWO56.

Several point scan measurements with grater magnification have been made of the precipitates, and the results give an amount of Ni that spans from 0,47 to 0,88 atomic percent. The precipitates in the bulk have a lower content of W, and the higher La content indicates that the bulk precipitates are La_2O_3 (Figure 4.20).

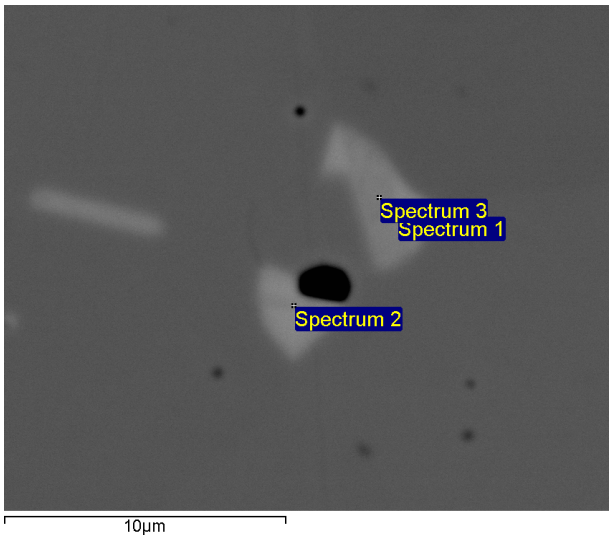

Spectrum	O [at%]	Ni [at%]	La [at%]	W [at%]
1	64,59	0,88	32,60	1,94
2	63,69	0,47	34,37	1,47
3	63,36	0,71	35,43	0,50

Figure 4.20 EDS analysis of precipitates in the bulk of La_2NiO_4 (100h).

X- ray element mapping of the diffusion couple are represented in Figure 4.21.

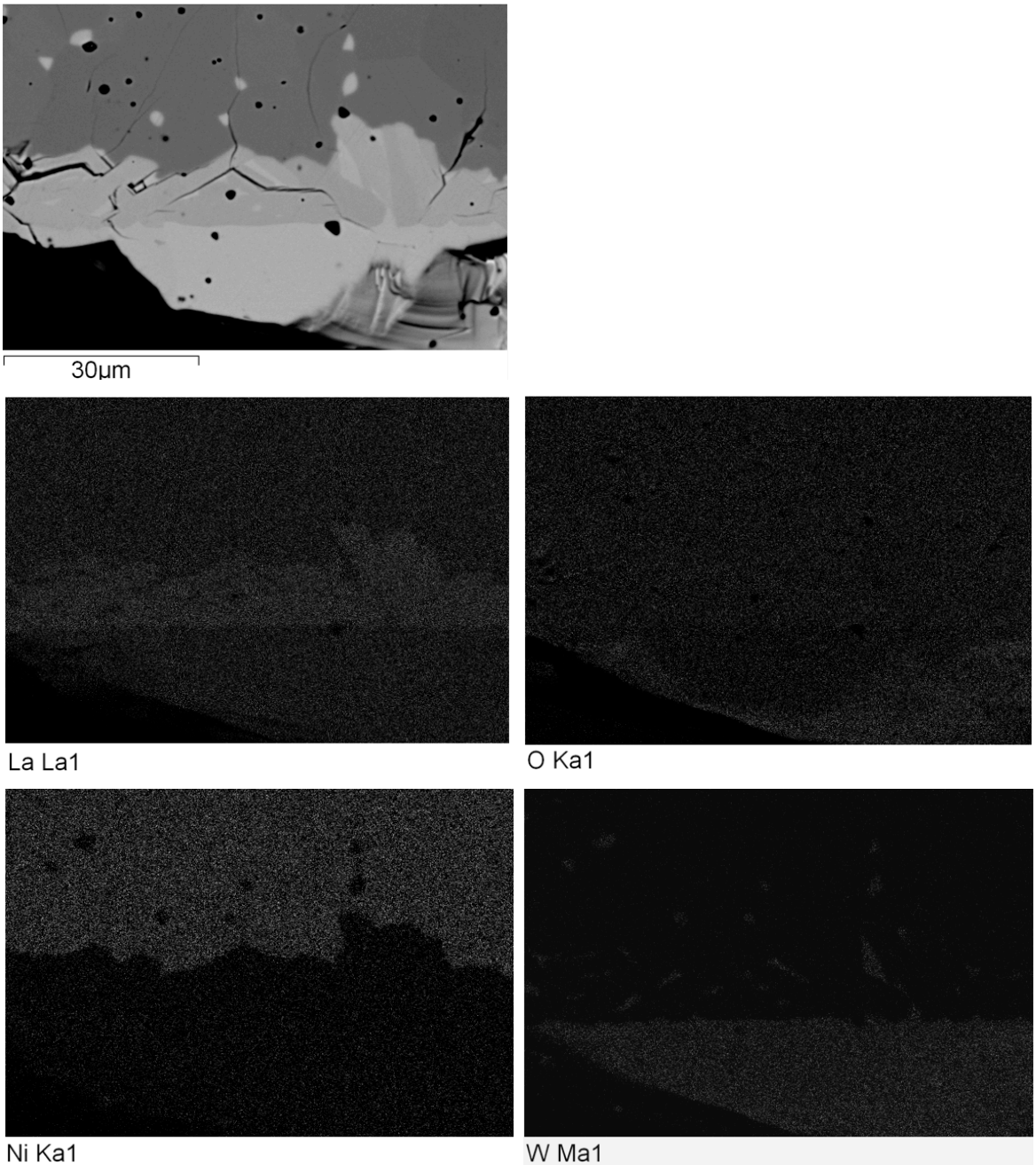

Figure 4.21 Element mapping of the diffusion couple fired for 100 hours at 1450°C in air. Maps are given for the elements: La, O, Ni and W.

Growth kinetics

Growth kinetics of the product layer is given graphically in Figure 4.22. The measured thickness of the product layer, x, follows the parabolic rate law

$$x^2 = 2k_p t + C \tag{4.1}$$

where k_p is the parabolic rate constant, t is the dwell time and C is an integration constant. The result indicate that the diffusion process is rate limiting and the kinetics is thus diffusion controlled.

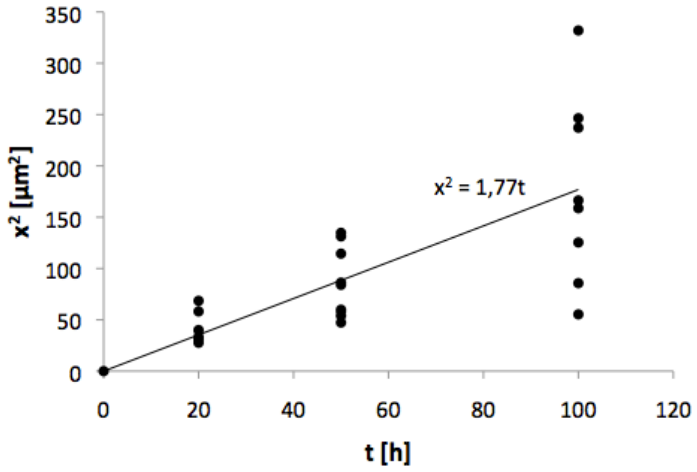

Figure 4.22 Parabolic plot of the thickness of the product layer versus the dwell time at 1450 °C in air

The parabolic rate constant k_p can be found from the linear regression in Figure 4.22. The slope of this plot yields a value of k_p equal to 0,885 µm²/h.

5. Discussion

5.1. Densification and microstructure

All samples were successfully sintered into dense pellets (Table 4.1). Density and microstructure for the $LaCoO_3$ pellets differ to some extent from the values reported elsewhere[21, 39]. Kleveland[21] states that a nearly 100 % dense material with an average grain size of 9 μm were obtained at 1350 °C. An explanation to the difference in microstructure and density can be agglomerates in the powder. The $LaCoO_3$ powder used in this study was synthesized by spray pyrolysis and calcination of the powder was necessary to obtain single phase. During calcination agglomerates formed and coarsening of the powder occurred. Agglomerates lead to heterogeneous packing of the green body, which in turn leads to differential sintering during the firing stage[40]. This can cause problems such as large pores and crack like voids. Furthermore, agglomerates affect the grain size in the microstructure. Ideally these agglomerates should have been broken down mechanically (e.g. milling) before pressing the powder into a green body.

An estimate of the grain size at the unpolished surfaces was found by the linear intercept method[38], and is only measured to give an indication of the grain-size. To find the true volume diameter of the grains polishing of the surface followed by etching will be necessary.

5.2. LWO56 – $LaCoO_3$ diffusion couples

Based on the marker experiment illustrated in Figure 5.1 and EDS results, an indication of what happens at the interface between $LaCoO_3$ and LWO56 can be known. In order to preserve local electro neutrality during the reaction and throughout the product it is necessary that, for every W^{6+} ions that diffuse, two Co^{3+} must diffuse in the opposite direction. This means that the $LaCo_{1-x}W_xO_3$/LWO interface moves faster and that the Co^{3+} ion diffusion dominates over the W^{6+} ion diffusion. Since the diffusion fluxes are different ($|J_{Co^{3+}}|>|J_{W^{6+}}|$) and there is a net flow of matter past the Pt-markers, the diffusion mechanism can only happen through vacancy diffusion[31].

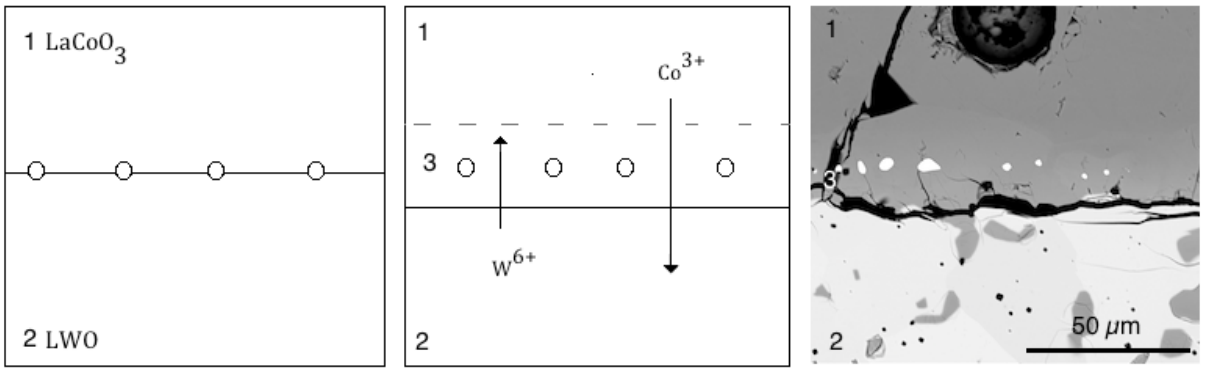

Figure 5.1 Principle of diffusion marker experiment sketched for the 50 h diffusion couple fired at 1450 °C in air. Phases: 1= $LaCoO_3$, 2 = LWO56, 3 $LaCo_{1-x}W_xO_3$. Platinum markers indicate the initial position of the interface between phase 1 and 2 after heat treatment.

It is believed that a reaction between the diffusive Co^{3+} and LWO56 occur at the initial interface and create a secondary phase of $LaCo_{1-x}W_xO_3$, which grows below the Pt-markers. The Co element in the $LaCoO_3$ phase is a 3d transition metal that can exhibit different valence states. When the perovskite-related $LaCo_{1-x}W_xO_3$ structure forms, a reduction of Co^{3+} to Co^{2+} is necessary to maintain electroneutrality. The same reduction happens when W^{6+} enters the $LaCoO_3$ structure and forms the same compound above the Pt-markers. The solubility, x, of W^{6+} has been proven to be 0.1 by solid-state reaction [41]. Figure 5.2 shows single phase $LaCo_{0.95}W_{0.05}O_3$ and $LaCo_{0.90}W_{0.10}O_3$.

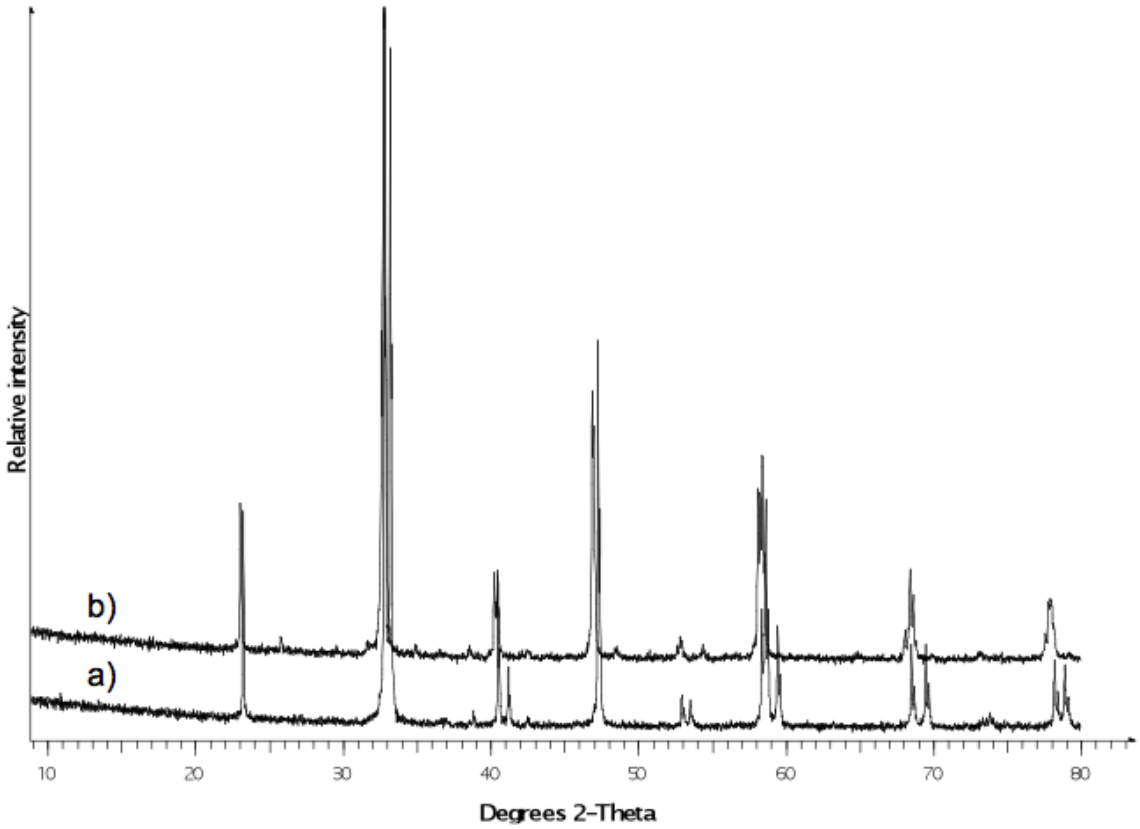

Figure 5.2 XRD pattern for single phase $LaCo_{1-x}W_xO_3$ made by solid- state reaction. (a) $LaCo_{0.95}W_{0.05}O_3$ and (b) $LaCo_{0.90}W_{0.10}O_3$ [41].

The $LaCo_{1-x}W_xO_3$ phase has also been synthesised for x values higher than 0,1. Subramanian[42] reported that a well defined single phase of $LaCo_{0.75}W_{0.25}O_3$ were easily formed under reducing conditions. The compound was black in colour and stable in air and in the presence of moisture. The compound did however decompose into $LaCoO_3$ and La_2O_3 phases at temperatures above 800 °C when heated in air.

Previously reactivity tests done by the author[43], including reaction of fine-grained powders and solid- state diffusion couples, confirmed the presence of a secondary phase of La_2O_3. The reactions were carried out at 1400 °C which make a temperature difference of 50 °C compared to the results reported here. XRD results are given in Figure 5.3. The transition of La_2O_3 into $La(OH)_3$ in Figure 5.3 is a consequence of the different time periods the samples were left in air before XRD scans. La_2O_3 is highly hygroscopic and the reaction of La_2O_3 into $La(OH)_3$ occur rapidly at room temperature.

The overall chemical reaction of the fine-grained powders can be written as

$$(1-x)LaCoO_3 + xLa_6WO_{12} = LaCo_{1-x}W_xO_3 + \frac{5}{2}xLa_2O_3 + \frac{3}{4}O_2 \qquad (5.1)$$

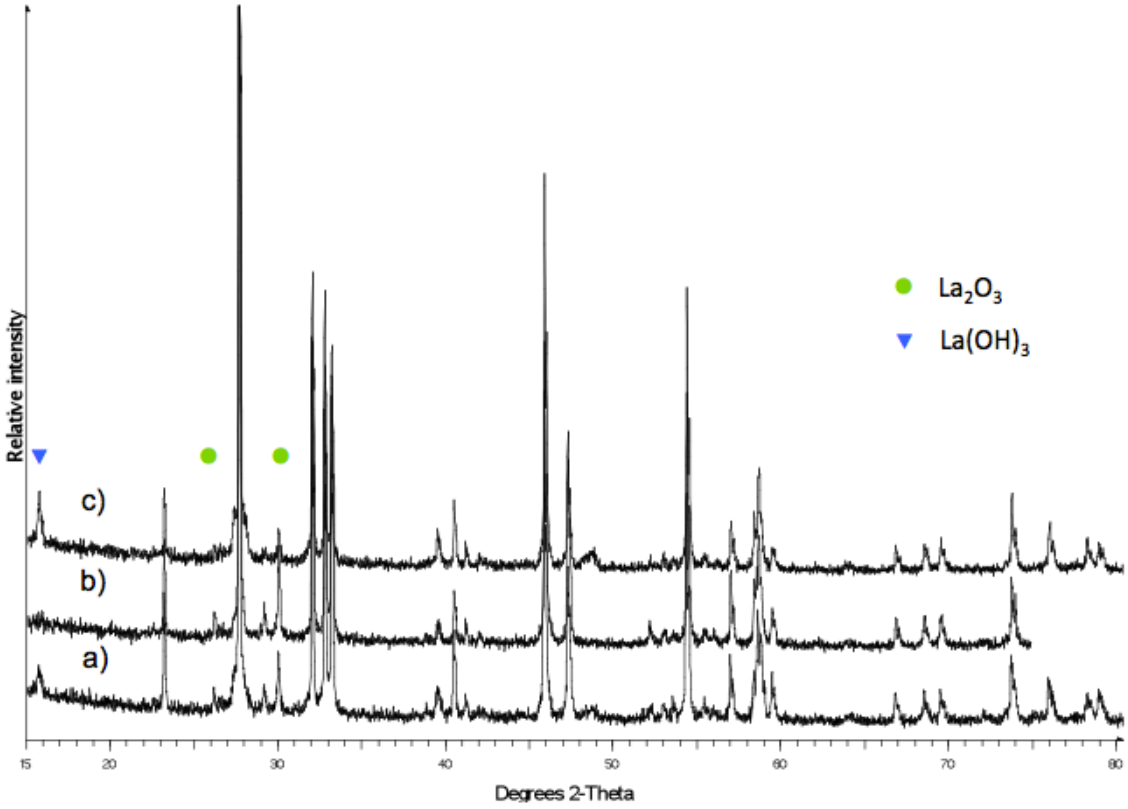

Figure 5.3 XRD pattern for the LWO56/$LaCoO_3$ diffusion couple after firing at 1400 °C for (a) 36 h, (b) 72 h and (c) 108 h. Peak position are shown for the phases: (●) La_2O_3 and (▼)$La(OH)_3$

The La_2O_3 phase in the solid- state diffusion couple could be seen between the initial phases down the whole length of the cross section. In difference from the results given here the solid state diffusion couple were formed by coating the polished LWO56 pellet with $LaCoO_3$ powder, and then fired at 1400 °C for 36 hours.[43] The reason why La_2O_3 is not formed in the diffusion couple studied in this thesis could relate to the competing pathway between the thermodynamic reaction and kinetic reaction. It is believed that selective formation of $LaCo_{1-x}W_xO_3$ will happen due to lower activation energy. This means that $LaCo_{1-x}W_xO_3$ is kinetically favoured while La_2O_3 is a thermodynamically controlled product.

The thermodynamically stability of the product formed at the interface is crucial for the device lifetime. Subramanian [42] states that $LaCo_{0.75}W_{0.25}O_3$ is unstable when heated above 800 °C in air. The formation of La_2O_3 has a detrimental effect due to its hygroscopic nature. La_2O_3 is also sensitive to other types of gases: methane, carbon monoxide and CO_2 molecules present in the surrounding atmosphere[44].

Growth kinetics of the product layer below the Pt-markers is illustrated in Figure 4.9. The thicknesses of the layer increases up to 50 h and then decrease from 50 to 100 h. The increase in thickness is assumed to happen due to the kinetics of the reaction. Since the trend in this area is linear it is believed that the process is diffusion controlled. A decrease in the thickness over time could then be a result of the reaction going towards equilibrium. A second explanation could be that the reaction is hindered due to phase separations at the LWO/$LaCo_{1-x}W_xO_3$ interface during heating. The phase separation may perhaps be caused by pressure that builds up on releasing O_2 (equation 5.1), or it can be an effect of the difference in thermal expansion between the two materials. Since the thickness of the product layer of the two diffusion couples that separated after heat treatment (20 and 100 h) are quite similar, the latter explanation is very plausible.

Precipitates in the LWO56 phase are found in all diffusion couples. It is possible that this phenomenon occur because the concentration of Co in LWO is above the solubility limit. At high temperatures Co^{3+} will diffuse from $LaCoO_3$ into LWO until equilibrium is established, and the solution so formed will be supersaturated when the diffusion couple is cooled. At lower temperatures (if the Co mobility is sufficient) the excess Co will precipitate. According to Ustinovshikov [45] the formation of precipitations in solid solutions can only happen by the spinodal mechanism. Since there is no thermodynamic barrier to the reaction inside the spinodal region, the decomposition is determined solely by diffusion. There is however some contradiction to the fact that the precipitates is formed solely by diffusion. Precipitates are distributed throughout the whole bulk of the LWO pellet and it is more likely that the formation happen trough another mechanism, but this warrants further investigation.

A consequence of the increasing amount of precipitates with time is that it in some way will affect the properties of the electrolyte. While the LWO material exhibit mixed ionic

and electronic conductivities[14], studies of the $LaCo_{0,75}W_{0,25}O_3$ phase in the range of 25-350°C shows that the precipitates formed here could have the properties of an extrinsic semiconductor[42].

Diffusion and reaction on the $LaCoO_3/Al_2O_3$ interface

Results indicates that Al diffuses into the $LaCoO_3$ pellet and react to form lanthanum aluminates species and CoO after heat treatment at 1450°C for 20, 50 (Figure 4.14) and 100 hours. Zhu [46] found that $LaAlO_3$ species was formed on the interface after heat treatment at 550 °C for 5 hours. The interaction between $LaCoO_3$ and Al_2O_3 were more serious when the heat treatment temperature was increased. The heating time could also intensify the interface diffusion. Since Al_2O_3 is a potential material for use in SOFC applications[47] it is of significance to mention that the diffusion and interaction between $LaCoO_3$ and Al_2O_3 could result in destruction of the perovskite structure[46].

5.3. LWO- La_2NiO_4 diffusion couples

The diffusion couples microstructure formed across the interface is summarized in the schematic drawing in Figure 5.4. The morphology and position of the product layer indicates that Ni^{2+} is the fastest diffusing specie. La_2NiO_4 is a Ruddlesden- Popper type phase described as stacked perovskite ($LaNiO_3$) layers alternating with rock-salt (La_2O_3) layers. [20] When Ni^{2+} ions are removed from this structure and solves in the LWO phase, La_2O_3 is formed as a secondary phase at the La_2NiO_4 side of the Pt-markers. At the same time W^{6+} diffuses into the La_2O_3 phase and react to form LWO. The fact that W^{6+} diffuses slower than Ni^{2+} is then visible since La_2O_3 is present at the interface. It is believed that the solubility of W^{6+} in La_2NiO_4 is low and most of the diffusing W^{6+} will be found in the product layer.

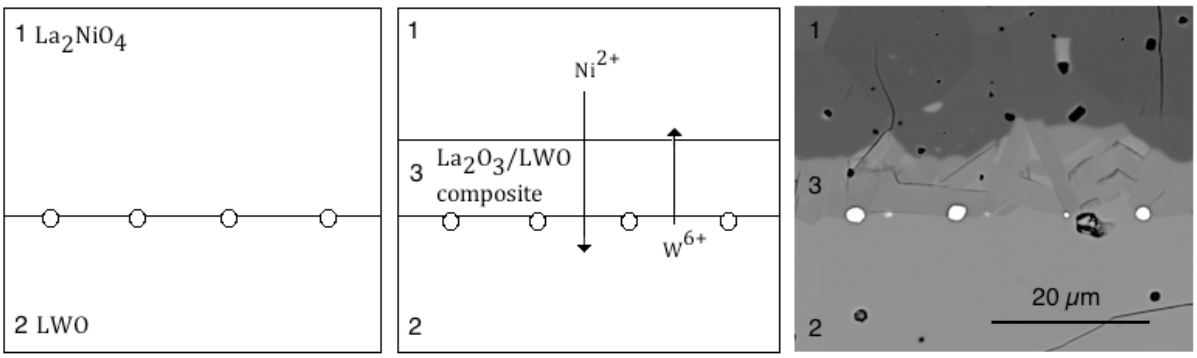

Figure 5.4 Principle of diffusion marker experiment sketched for the 50 h diffusion couple fired at 1450 °C in air. Phases: 1= La_2NiO_4 , 2 = LWO56, 3 La_2O_3 /LWO composite. Platinum markers indicate the initial position of the interface between La_2NiO_4 and LWO56 after heat treatment.

Hardly any nickel was found close to the interface (Figure 4.17 and Figure 4.18), but this does not prove that Ni^{2+} does not diffuse. If Ni^{2+} is well solved in the LWO structure, Ni^{2+} could be hard to detect. However the moving boundary implies that Ni^{2+} disappear from the La_2NiO_4 structure. It is not believed that Ni^{2+} will diffuse against the chemical potential gradient since diffusion occurs so as to minimise the free energy[34, 48].

Since W^{6+} is the slowest diffusing specie and has a low solubility in the La_2NiO_4 structure the product layer will continue to grow as a La_2O_3/LWO composite until it reach a

critical thickness[34]. The characteristic needle shaped La_2O_3/LWO composite layer is a result of either (1) the anisotropic La_2NiO_4 structure[49] or (2) the hexagonal structure of La_2O_3 [50]. The growth is diffusion controlled and follows the parabolic law. In this case the rate of the growth of the layer is inversely proportional to its total thickness, x, existing at a time t [34].

The XRD spectrum of 1:1 mixtures by mass of LWO56 and La_2NiO_4 powders is present in Figure 5.5. The result gives an indication of what will happen with the composite layer when time passes. The spectrums are identical which means that equilibrium is reached between the reacting phases, and all La_2O_3 has reacted into LWO.

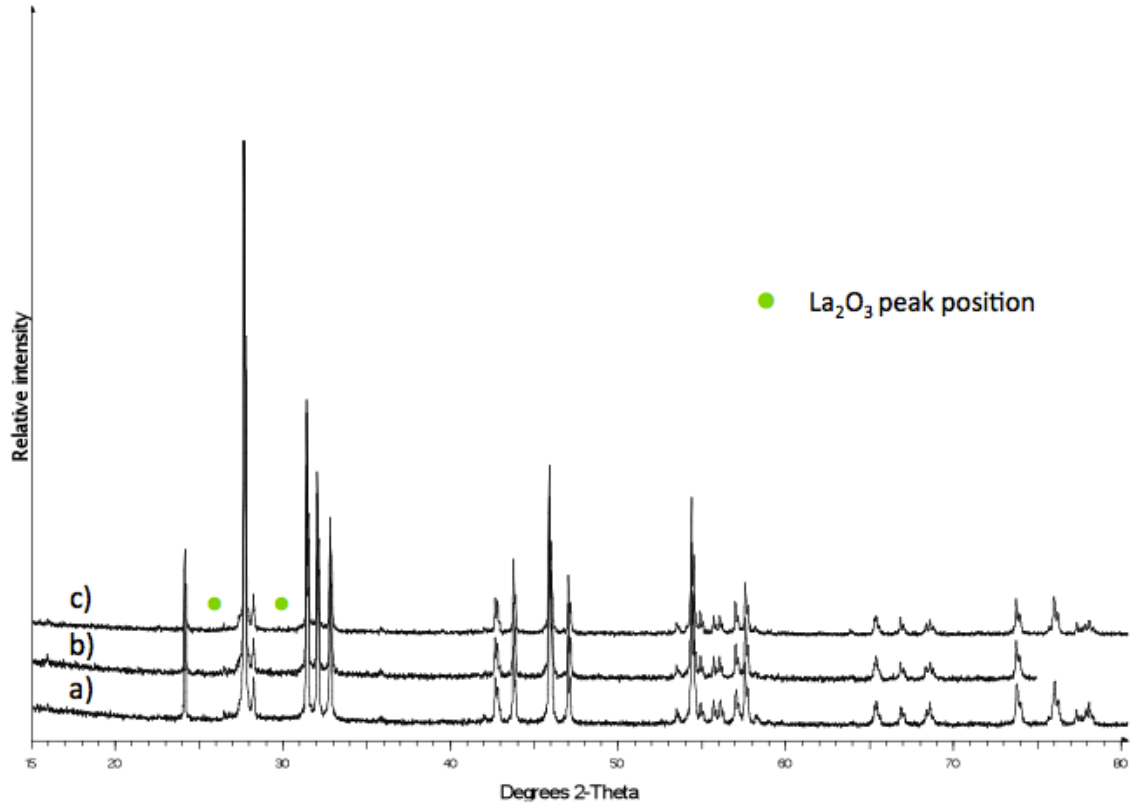

Figure 5.5 XRD pattern for the LWO56/La_2NiO_4 diffusion couple after firing at 1400 °C for (a) 36 h, (b) 72 h and (c) 108 h. No peaks are visible for the phase (●) La_2O_3.[43]

Precipitates of LWO were found in the La_2NiO_4 phase in all diffusion couples. Point scan measurements close to the interface (Figure 4.19) indicated small amounts of nickel in the precipitates. It is however uncertain if the detected amount is from the surrounding matrix or if it is solvated nickel in the LWO phase. Further into the La_2NiO_4 bulk the content of tungsten in the precipitates decrease (Figure 4.20). The La/W ratio is high

which indicate that the precipitates in the bulk are La_2O_3. The fact that the shape of the precipitate changes from more spherical close to the interface to needle shaped in the bulk, support the indication of two different precipitate phases.

5.4. Thermal expansion

Cobaltite based cathodes are known to have high thermal expansion coefficients (TEC)[1] which complicate the matching of partner materials, and the use of $LaCoO_3$ with LWO shows no exception. Poor adherence or interfacial cracking is observed for all diffusion couples with $LaCoO_3$ as cathode material. In the case of La_2NiO_4 as cathode material the phase remaines well connected to the LWO when heat-treated for 50 hours (Figure 4.15). The reason why the diffusion couples fractured after heat treatment at 20 and 100 hours could have been related to the change in load, which was decreased after the first experiment (50h). A second error could be the balance of the load, which was placed on top of two diffusion couples (front Figure 3.1). Since the pellets differed in size it was hard to ensure uniform distribution of the weight. A third factor is La_2O_3, which can react with air and expand at the interface.

The difference in thermal expansion during heating could cause cracking or warping in the fuel cell, which could lower the lifetime. If the fuel cell survives the heating to operation temperature without significant stress, the TEC values are similar to such an extent that problems with thermal expansion could be non-existent.[51] Available thermal expansion data for the cathode materials investigated here is listed in Table 5.1.

Table 5.1 Linear thermal expansion coefficients (TEC) for materials used in this study

Composition	Temperature range [K]	TEC [K^{-1}]
$LaCoO_3$ [24, 52]	RT-1100	$20\text{-}23 \cdot 10^{-6}$
La_2NiO_4 [26]	348-1173	$13{,}8 \cdot 10^{-6}$
LWO56[53]	RT-1200	$12{,}1 \cdot 10^{-6}$

6. Conclusions

A solid-solid diffusion couple experimental technique was used for studying the reaction of La_6WO_{12} (La/W=5,6) with $LaCoO_3$ and La_2NiO_4. Dense single-phase pellets were coupled with inert platinum markers at the interface and heat treated at 1450 °C for various times. Based on the results of this study the following can be concluded.

The solid- state reaction between La_6WO_{12} and $LaCoO_3$ showed formation of a secondary phase of $LaCo_{1-x}W_xO_3$ at the interface and as precipitates in the La_6WO_{12} phase. The cation diffusion was predicted from the position of the Pt- markers and showed that diffusion of Co cations dominates over W^{6+}. The solubility, x, of W^{6+} in the $LaCo_{1-x}W_xO_3$ structure was analysed by EDS and was found to be lower and equal to 0,1. The reaction kinetics of the product layer failed to fit the theoretical models, which is either diffusion controlled or interface controlled. The reason for the failure could relate to the fact that the reaction goes towards equilibrium after a certain firing time, or poor connectivity between the reacting materials during heating.

In the case of La_2NiO_4 as a cathode material a composite layer of La_6WO_{12} and La_2O_3 was formed at the interface. The reaction kinetics of the product layer was a diffusion-controlled process where diffusion of Ni^{2+} dominates over W^{6+}. In addition to the interface reaction EDS analysis indicated precipitate formation in the La_2NiO_4 phase. More rounded precipitates of La_6WO_{12} was found close to the interface while formation of needle shaped La_2O_3 precipitates were found in the bulk.

All in all, the stability and compatibility between La_6WO_{12} and the potential cathode materials $LaCoO_3$ and La_2NiO_4 is not looking good. The formation of $LaCo_{1-x}W_xO_3$ precipitates throughout the electrolyte is expected to influence the transport properties and hence the ionic conduction. An investigation of the stability of this phase is also necessary since decomposition into La_2O_3 is detrimental. In addition to high reactivity, $LaCoO_3$ shows challenges in the combination with La_6WO_{12} due to a high thermal expansion coefficient. In the case of La_2NiO_4 as cathode material the formation of La_2O_3

will result in serve degradation with increasing time of cell operation due to the hygroscopic nature of the material.

References

1. Singhal, S.C. and K. Kendall, *High-temperature solid oxide fuel cells: fundamentals, design, and applicatons*. 2003, New York: Elsevier Advanced Technology.
2. Haile, S.M., *Materials for fuel cells.* Materials Today, 2003. **6**(3): p. 24-29.
3. Tolchard, J., *ELECTROLYTES | Solid: Protons*, in *Encyclopedia of Electrochemical Power Sources*. 2009, Elsevier: Amsterdam. p. 188-195.
4. Tolchard, J.R., H.L. Lein, and T. Grande, *Chemical compatibility of proton conducting LaNbO4 electrolyte with potential oxide cathodes.* Journal of the European Ceramic Society, 2009. **29**(13): p. 2823-2830.
5. Quadakkers, W.J., et al., *Metallic interconnectors for solid oxide fuel cells - a review.* Materials at high temperatures, 2003. **20**(2): p. 115-127.
6. Malavasi, L., C. Ritter, and G. Chiodelli, *Correlation between Thermal Properties, Electrical Conductivity, and Crystal Structure in the BaCe0.80Y0.20O2.9 Proton Conductor.* Chemistry of Materials, 2008. **20**(6): p. 2343-2351.
7. Magrasó, A., et al., *Development of Proton Conducting SOFCs Based on LaNbO4 Electrolyte – Status in Norway.* Fuel Cells, 2011. **11**(1): p. 17-25.
8. Larminie, J. and A. Dicks, *Fuel cell systems explained*. 2003, Chichester: Wiley. xxii, 406 s.
9. Kendrick, E., et al., *Cooperative mechanisms of fast-ion conduction in gallium-based oxides with tetrahedral moieties.* Nature materials, 2007. **6**(11): p. 871-875.
10. Kreuer, K.D., *Proton-conducting oxides.* Annual Review of Materials Research, 2003. **33**: p. 333-359.
11. Tao, S. and J.T.S. Irvine, *A Stable, Easily Sintered Proton- Conducting Oxide Electrolyte for Moderate-Temperature Fuel Cells and Electrolyzers.* Advanced Materials, 2006. **18**(12): p. 1581-1584.
12. Haile, S.M., *Fuel cell materials and components.* Acta Materialia, 2003. **51**(19): p. 5981-6000.

13. Lein, H.L., et al., *Asymmetric proton conducting oxide membranes and fuel cells prepared by aqueous tape casting.* Solid State Ionics, 2008. **179**(21-26): p. 1146-1150.
14. Haugsrud, R. and C. Kjølseth, *Effects of protons and acceptor substitution on the electrical conductivity of La6WO12.* Journal of Physics and Chemistry of Solids, 2008. **69**(7): p. 1758-1765.
15. Magraso, A., et al., *New crystal structure and characterization of lanthanum tungstate "La6WO12" prepared by freeze-drying synthesis.* Dalton Transactions, 2009(46): p. 10273-10283.
16. Hage, F.S., *A structural investigation of erbium titanate and lanthanum tungstate by CBED*. 2009, F.S. Hage: Oslo.
17. Haugsrud, R., *Defects and transport properties in Ln6WO12 (Ln=La, Nd, Gd, Er).* Solid State Ionics, 2007. **178**(7-10): p. 555-560.
18. Haugsrud, R. and T. Nordby, *Proton conduction in rare-earth ortho-niobates and ortho-tantalates.* Nature materials, 2006. **5**(3): p. 193-196.
19. Hernández, A.M., L. Mogni, and A. Caneiro, *La2NiO4+[delta] as cathode for SOFC: Reactivity study with YSZ and CGO electrolytes.* International Journal of Hydrogen Energy, 2010. **35**(11): p. 6031-6036.
20. Shen, Y., et al., *Preparation and electrical properties of Ca-doped La2NiO4+d cathode materials for IT-SOFC.* Physical Chemistry Chamical Physics, 2010. **12**: p. 15124-15131.
21. Kleveland, K., *Preparation, microstructure and mechanical properties of $LaCoO_3$ and $SrFeO_3$ based ceramics*. 2000, [Tapir]: Trondheim.
22. Orlovskaya, N., et al., *Mechanical properties of LaCoO3 based ceramics.* Journal of the European Ceramic Society, 2000. **20**(1): p. 51-56.
23. Cava, R.J.; Available from: http://www.princeton.edu/~cavalab/tutorials/public/structures/perovskites.html.
24. Radovic, M., et al., *Thermal, mechanical and phase stability of LaCoO3 in reducing and oxidizing environments.* Journal of Power Sources, 2008. **184**(1): p. 77-83.
25. Burns, G., et al., *Low-temperature structural phase transition in La_{2}NiO_{4+ delta }.* Physical Review B, 1990. **42**(16): p. 10777.
26. Skinner, S.J., *Characterisation of La2NiO4+[delta] using in-situ high temperature neutron powder diffraction.* Solid State Sciences, 2003. **5**(3): p. 419-426.

27. Heulens, J., B. Blanpain, and N. Moelans, *Phase-field analysis of a ternary two-phase diffusion couple with multiple analytical solutions.* Acta Materialia, 2011. **59**(10): p. 3946-3954.

28. Leaist, D.G. and H. Mehrer, *Diffusion*. 2008, AccessScience, McGraw-Hill Companies, www.accessience.com.

29. Askeland, D.R., et al., *The science and engineering of materials*. 2011, Stamford, Conn.: Cengage Learning. XXIII, 920 s.

30. Palcut, M., *Cation diffusion in $LaMnO_3$, $LaCoO_3$ and $LaFeO_3$ materials*. 2007, Norwegian University of Science and Technology, Faculty of Natural Sciences and Technology, Department of Materials Science and Engineering: Trondheim. p. VI, 142, [20] s.

31. Gao, W. and N.M. Sammes, *An Introduction to Electronic and Ionic Materials*. 2000, Singapore: World Scientific Publishing Co. Pte. Ltd.

32. Gosele, U. and K.N. Tu, *Growth kinetics of planar binary diffusion couples: "Thin film case" versus "bulk cases".* Journal of Applied Physics, 1982. **53**(4): p. 3252-3260.

33. Tilley, R.J.D., *Understanding solids: the science of materials*. 2004, Chichester, West Sussex, England: J. Wiley. xxii, 593 s.

34. Dybkov, V.I., *Reaction diffusion and solid state chemical kinetics*. 2002, Kyiv: IPMS Publications. XVII, 298 s.

35. ISO, *Dense shaped refractory products- Determination of bulk density, apparent porosity and true porosity*. 1998.

36. Radaelli, P.G. and S.W. Cheong, *Structural phenomena associated with the spin-state transition in LaCoO3.* Physical Review B, 2002. **66**(9): p. 094408.

37. J.-C. Park, D.-K.K., S.-H. Byeon and D. Kim, *XANES study on Ruddlesden-Popper phase, Lan+1NinO3n+1 (n = 1, 2, and).* Journal of Synchrotron Radiation, 2001. **8**(Part 2): p. 704-706.

38. Thompson, A.W., *Calculation of true volume grain diameter.* Metallography, 1972. **5**(4): p. 366-369.

39. Panneerselvam, M. and K.J. Rao, *Microwave preparation and sintering of industrially important perovskite oxides: LaMO3 (M = Cr, Co, Ni).* Journal of Materials Chemistry, 2003. **13**(3): p. 596-601.

40. Rahaman, M.N., *Ceramic processing and sintering*. 1995, New York: Marcel Dekker. XI, 770 s.
41. Karas, F., *Chemical compatibility of interfaces in proton conducting fuel cells*. 2011, Department of Material Science and Technology, NTNU: Trondheim.
42. Subramanian, M.A. and G.V. Subba Rao, *Synthesis and electrical properties of perovskite oxides, LnB0.75B'0.25O3.* Journal of Solid State Chemistry, 1980. **31**(3): p. 329-335.
43. Bjørnevik, I.M., *Stability and compatibility of cathodes in proton conducting SOFCs*. 2010, Department of Materials Science and Engineering Trondheim.
44. Bakiza, B., et al., *Elaboration, Characterization Of LaOHCO3, La2O2CO3 And La2O3 Phases And Their Gas Solid Interactions With CH4 And CO Gases.* M. J. Condensed matter, 2010. **12**(1): p. 60-67.
45. Ustinovshikov, Y.I., *Precipitation in solids.* Journal of Materials Science, 1992. **27**(15): p. 3993-4002.
46. Zhu, Y., R. Tan, and L. Cao, *Study of the interface action between LaCoO3 layer and Al2O3 substrate.* Surface and Interface Analysis, 2001. **32**(1): p. 183-188.
47. Sang, S., et al., *Novel Al2O3-based compressive seals for IT-SOFC applications.* Journal of Power Sources, 2008. **177**(1): p. 77-82.
48. Baierlein, R., *The elusive chemical potential.* American Journal of Physics, 2000. **69**(4): p. 423-434.
49. Bassat, J.M., et al., *Anisotropic ionic transport properties in La2NiO4+[delta] single crystals.* Solid State Ionics, 2004. **167**(3-4): p. 341-347.
50. Lal, H.B. and K. Gaur, *Electrical conduction in non-metallic rare-earth solids.* Journal of Materials Science, 1988. **23**(3): p. 919-923.
51. Øygarden, V., *LaNb1/3M2/3O3 (M = Ni, Co, Cu) cathodes in fuel cells based on proton conducting LaNbO4 electrolyte.* 2009, Department of Material Science and Engineering, NTNU: Trondheim.
52. Kharton, V.V., et al., *Mixed electronic and ionic conductivity of LaCo(M)O3 (M=Ga, Cr, Fe or Ni): IV. Effect of preparation method on oxygen transport in LaCoO3-[delta].* Solid State Ionics, 2000. **138**(1-2): p. 135-148.
53. Hernández, V.G., *Sintered rod, 97% theor. Rel. density, 25mm lenght*. 2011, NTNU.